



29 **One Sentence Summary:** SARS-CoV-2 infected mink develop severe respiratory disease that  
30 recapitulates some components of severe acute respiratory disease, including ARDS.

31

32 **Abstract:**

33 An animal model that fully recapitulates severe COVID-19 presentation in humans has been a  
34 top priority since the discovery of SARS-CoV-2 in 2019. Although multiple animal models are  
35 available for mild to moderate clinical disease, a non-transgenic model that develops severe  
36 acute respiratory disease has not been described. Mink experimentally infected with SARS-CoV-  
37 2 developed severe acute respiratory disease, as evident by clinical respiratory disease,  
38 radiological, and histological changes. Virus was detected in nasal, oral, rectal, and fur swabs.  
39 Deep sequencing of SARS-CoV-2 from oral swabs and lung tissue samples showed repeated  
40 enrichment for a mutation in the gene encoding for nonstructural protein 6 in open reading frame  
41 1a/1ab. Together, these data indicate that American mink develop clinical features characteristic  
42 of severe COVID19 and as such, are uniquely suited to test viral countermeasures.

43

44

45

46 **Keywords:** SARS-CoV-2, mustelid, mink, ARDS, COVID-19

47

## 48 INTRODUCTION

49 Development of animal models has been a critical need since the emergence of SARS-  
50 CoV-2 in order to test vaccines and viral countermeasures (1). Multiple SARS-CoV-2 models of  
51 traditional laboratory species, including mice, hamsters, ferrets, and nonhuman primates, have  
52 been developed (2-6). However, these models either result in mild to moderate disease or  
53 experience distinctive viral dissemination due to altered angiotensin-converting enzyme 2  
54 (ACE2) expression, specifically in the brain (2,3,6). An animal model that duplicates the severe  
55 acute disease spectrum of COVID-19 is still needed. Such a model would allow experimental  
56 research into the pathogenesis of severe COVID-19 and would facilitate the evaluation of  
57 therapeutic countermeasures in the context of severe disease.

58 Experimental infections of ferrets resulted in viral replication and transmission to naïve  
59 individuals, but very minimal to mild clinical signs of disease (4,5). However, this does not  
60 appear to be the case for all members of the Mustelidae family (4,5,7-9). Reports of farmed mink  
61 (*Neovison vison*) infected with SARS-CoV-2 emerged in the Netherlands in April 2020 (10). To  
62 date, at least 12 countries have reported outbreaks in farmed mink, as well as two reports  
63 describing positive feral or escaped mink (11,12). While many naturally infected mink exhibited  
64 mild to moderate clinical disease, a subset of these animals experienced an acute interstitial  
65 pneumonia that manifested with severe respiratory distress (10,13). Genomic surveillance in  
66 samples originating from mink in Denmark identified a series of changes in SARS-CoV-2 spike  
67 protein, known as the Cluster 5 variant (14). This mink-associated variant resulted in reduced  
68 neutralization with human convalescent sera *in vitro* (14). A high susceptibility to infection  
69 coupled with the public health risk of intra-host viral evolution prompted massive culls of an  
70 estimated 17 million mink on Danish farms (15).

71 Here, we show that experimentally infected mink develop a severe acute respiratory  
72 infection. After infection, progressive respiratory disease can be observed clinically,  
73 radiographically, and by histopathology. High amounts of viral RNA and infectious virus can be  
74 detected from the respiratory tract. Deep sequencing of SARS-CoV-2 genomes from oral swabs  
75 and lung tissue samples collected 3 days post-inoculation demonstrate rapid enrichment for a  
76 nonsynonymous mutation in the gene encoding for the nonstructural protein 6 (*nsp6*) in ORF1a  
77 in lung tissue samples. These data indicate the potential for rapid viral evolution in mink at the  
78 human-animal interface in a short timeframe. Together, these data suggest that the mink animal  
79 model recapitulates severe disease observed in hospitalized and fatal human cases of COVID-19  
80 and could be useful to test countermeasures against severe COVID-19.

## 81 RESULTS

### 82 Mink ACE2 supports efficient entry of SARS-CoV-2

83 To evaluate the utility of the mink model for COVID-19, we compared human and mink  
84 ACE2 functional receptor entry using structural analysis and a vesicular stomatitis virus  
85 pseudotype entry assay (16). The sequence of mink (*Neovison vison*) ACE2 was obtained by  
86 sequencing from lung tissue. The obtained mink ACE2 sequence is 99.8% identical to the  
87 previously published *Neovison vison* ACE2 sequence (GenBank QPL1221.1). Two substitutions  
88 are observed at residues 231 and 613, in which the threonine and tyrosine in the previous  
89 sequence are replaced by a lysine and a cysteine, respectively. These residues are not located in  
90 the SARS-CoV-2 receptor binding domain (RBD)-ACE2 interface. Both American mink ACE2  
91 sequences are 99% identical to the published European mink ACE2 sequence (*Mustela lutreola*  
92 *biedermanni*, GenBank QNC68911.1), and ~83% identical to human ACE2 (*Homo sapiens*,  
93 GenBank BAB40370.1) (Figure 1A).

94 To compare differences within the ACE2 interface with the SARS-CoV-2 spike receptor  
 95 binding domain (RBD), the residues participating in the interaction, as described by Lan, *et al.*

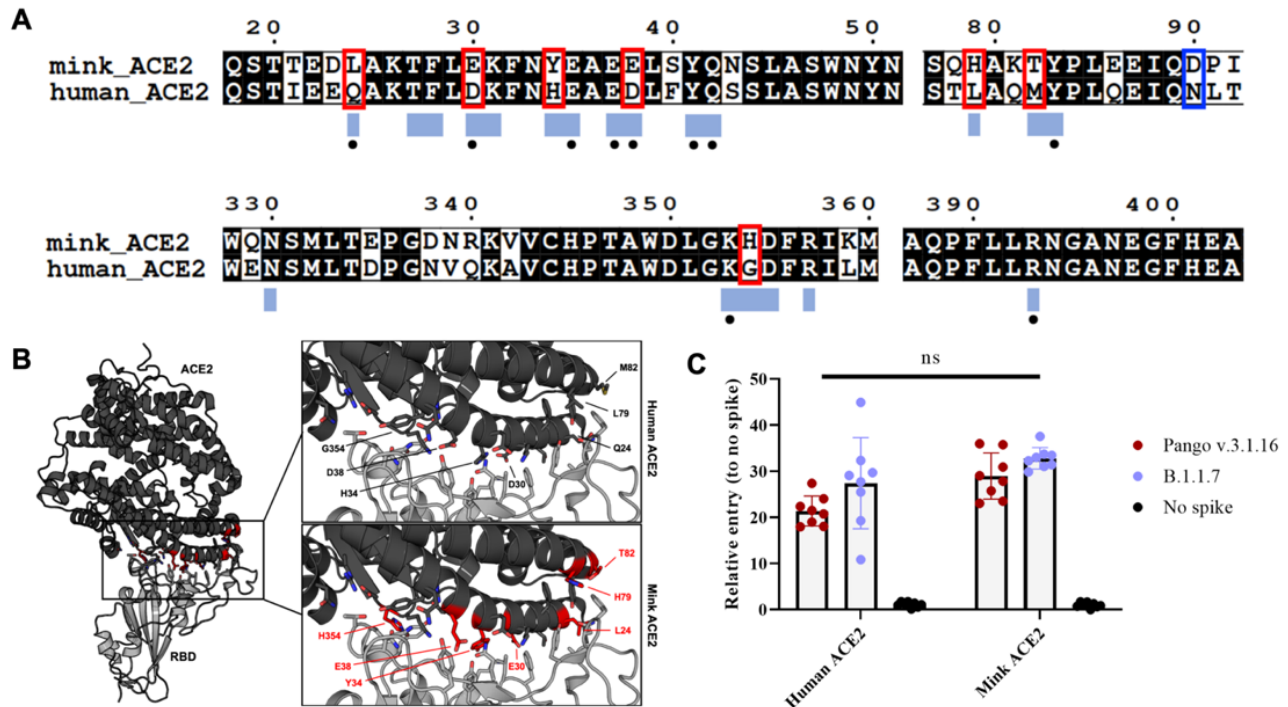


**Figure 1. Functional SARS-CoV-2 entry analysis with human and mink ACE2.** (A) An amino acid sequence alignment of ACE2 from the mink and human. Residues that participate in the SARS-CoV-2 RBD – ACE2 interaction are noted below the alignment by a blue box. Residues that participate in intermolecular hydrogen bonding or salt bridges are marked with a black dot. ACE2 residues that differ between mink and human within the interface are outlined with a red box. The substitution at residue 90 affecting an N-linked glycosylation site is noted with a blue box. (B) Differences between mink and human ACE2 are highlighted on the structure of the complex of SARS-CoV-2 RBD in gray bound to human ACE2 in black. Sidechains of the ACE2 and RBD residues that participate in the binding interaction are shown as sticks. The mutated residues are indicated by red. (C) SARS-CoV-2 spike pseudotype assay showing relative entry compared to no spike control in BHK cells expressing human or mink ACE2. Bars depict standard deviation.

96 (17), were mapped onto an amino acid sequence alignment of ACE2 from American mink  
 97 (*Neovison vison*), European mink (*Mustela lutreola biedermani*, GenBank QNC68911.1), and  
 98 humans (*Homo sapiens*, GenBank BAB40370.1)(18). The binding residues are 65% identical  
 99 between mink and human ACE2, with seven of the 20 total interface residues differing in mink  
 100 (Figure 1A). These residues are highlighted on the structure of SARS-CoV-2 RBD bound to

101 human ACE2 to visualize these differences (Figure 1B). Consistent with a previous analysis,  
102 critical residues for interaction with the spike RBD, K31, Y41, and Y353 are conserved (18).

103 To investigate if the observed discrepancies between human and mink ACE2 translates to  
104 significant differences in spike entry, we directly compared the viral entry of VSV SARS-CoV-2  
105 spike pseudotype particles on Baby Hamster Kidney fibroblasts (BHK cells) transfected with  
106 either human or mink ACE2. We observed significantly increased entry in mink ACE2 expressing  
107 cells compared to those expressing human ACE2 for the prototype WA1 lineage A SARS-CoV-2  
108 spike (Figure 1C, alignment, entry data,  $p = 0.0307$ , 2-way ANOVA followed by Šídák's multiple).  
109 However, the B.1.1.7 (Alpha) variant showed no difference ( $p = 0.1505$ , 2way ANOVA followed  
110 by Šídák's multiple). Overall, the Alpha variant showed increased entry in both human and mink  
111 ACE2. Considering both variants together, there was no statistical difference in entry of the spikes  
112 to human and mink ACE2 ( $p = 0.5633$ , Two-tailed t-test) (Figure 1C).

113 We next determined the ACE2 expression in the respiratory tract of mink. ACE2 was  
114 multifocally detected in the respiratory olfactory epithelium and there were multifocal SARS-  
115 CoV-2 immunoreactive respiratory and olfactory epithelial cells (Supplemental Figure 1). ACE2  
116 immunoreactivity was also detected in the lower respiratory bronchiolar epithelium and type I  
117 and type II pneumocytes (Supplemental Figure 1, D, E).

### 118 **Experimentally infected mink develop severe respiratory disease by 2 days post inoculation**

119 Eleven adult farmed mink were inoculated intranasally and intratracheally with  $10^5$   
120 TCID<sub>50</sub> of Alpha Variant, B.1.1.7 (hCoV-319 19/England/204820464/2020, EPI\_ISL\_683466).  
121 Due to the severity of clinical disease and respiratory distress, two animals reached end-point  
122 criteria and were euthanized the evening of 2 days post-inoculation (DPI). Eight animals reached

123 end-point criteria on 3 DPI, and one animal recovered from severe disease and was euthanized  
124 on the predetermined experimental endpoint of 28 DPI.

125         Marked weight loss (up to 15%) was observed in all animals by 3 DPI (Figure 2A). In  
126 the animal that survived infection, bodyweight returned to baseline values by 14 DPI  
127 (Supplemental Figure 2A). Clinical signs were first detectable on 1 DPI in 5 of 11 (45 %)  
128 animals, with clinical signs observed in 9 of 11 (82 %) animals by 2 DPI and all remaining  
129 animals by 3 DPI. Signs of clinical disease included dull mentation, shivering, hunched or balled  
130 posture, lethargy, anorexia, increased respiratory effort, tachypnea, with occasional nasal  
131 discharge that included both epistaxis and serous discharge (Figure 2). Animals were examined  
132 on 1,3, 5, 7, 10, 14, 17, 21, and 28 DPI under anesthesia; 10 animals were clinically dehydrated  
133 by 3 DPI.

134         Complete blood count (CBC) and complete chemistry panels were performed on blood  
135 samples collected at least one week prior to infection and at 0, 1, 3, 5, 7, 10, 14, 17, 21, and 28  
136 DPI. At all time-points post infection, the CBC was unremarkable apart from a decreased white  
137 blood cell (WBC) count characterized by a mild lymphopenia that was most pronounced in the 9  
138 remaining animals on 3 DPI (Figure 2C). The neutrophil-to-lymphocyte ratio was significantly  
139 increased at the terminal endpoint for clinically ill animals (Figure 2D). The single surviving  
140 animal had an elevated neutrophil-to-lymphocyte ratio (NLR) that peaked on 5 DPI as compared  
141 to baseline then quickly decreased (Supplemental Figure 2B). The blood chemistry panel was  
142 clinically unremarkable for all values except for a mild hypoproteinemia and hypoalbuminemia  
143 (Figure 2E).

144

145

146

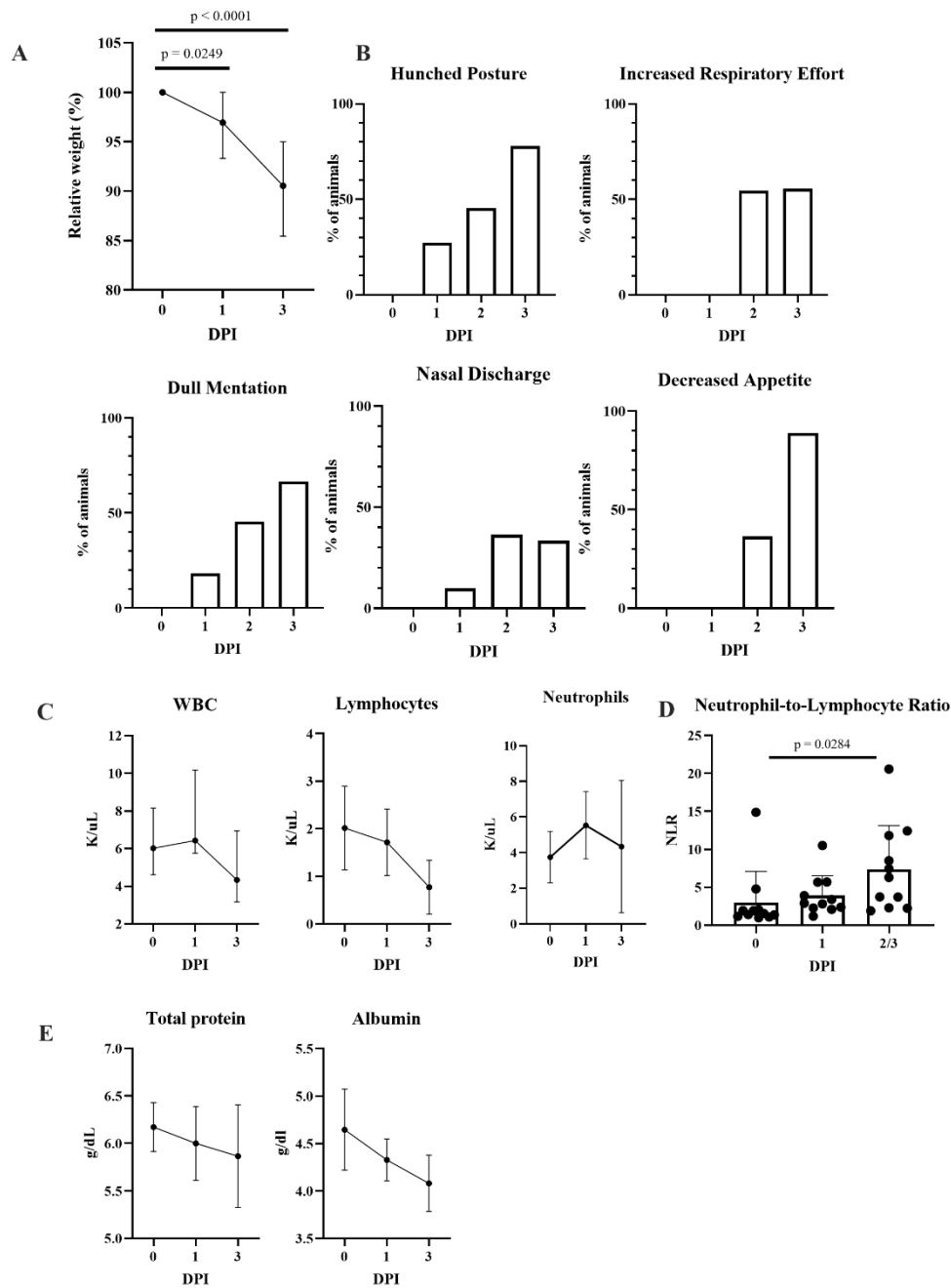


**Figure 2. Features of acute respiratory disease in mink.** (A) Percent of original body weight was collected during clinical exams on 1 and 3 DPI. Mink lost a significant amount of body weight on both 1 and 3 DPI (One-way ANOVA with Tukey's multiple comparisons test). (B) Mink were assessed at least twice daily and evaluated for hunched posture, respiratory effort, mentation, nasal discharge, and appetite. (C) Complete blood count values collected after infection. The median with the 95% confidence interval (CI) are depicted. (D) Increased Neutrophil-to-Lymphocyte Ratio as determined from the complete blood count. Mean with standard deviation depicted, 2-way ANOVA with Tukey's multiple comparisons test. (E) Selected blood chemistry values, median with 95% CI depicted.



## 147 **Progressive pulmonary infiltrates evident in pulmonary radiographs**

148 Radiographic scores on 1 and 3 DPI were increased as compared to baseline values

149 (Figure 3A) and indicated the presence of progressive pulmonary infiltrates consistent with viral

150 pneumonia likely with concurrent non-cardiogenic pulmonary edema secondary to acute

151 respiratory disease syndrome (ARDS)(Figure 3B). On 1 DPI, radiographic changes consistent

152 with viral pneumonia were present in the thoracic radiographs of 5 (45%) of 11 mink. Of these 5,

153 4 had evidence of a mild-to-moderate ground glass/unstructured interstitial pattern and the

154 remaining animal had a moderate-to-marked alveolar pattern affecting multiple lung lobes.

155 Interestingly, this animal had progressive multifocal grade 3 and 4 pulmonary infiltrates at 2 DPI

156 prior to euthanasia (Figure 3). At 3 DPI, 8 of the 9 remaining animals displayed disease

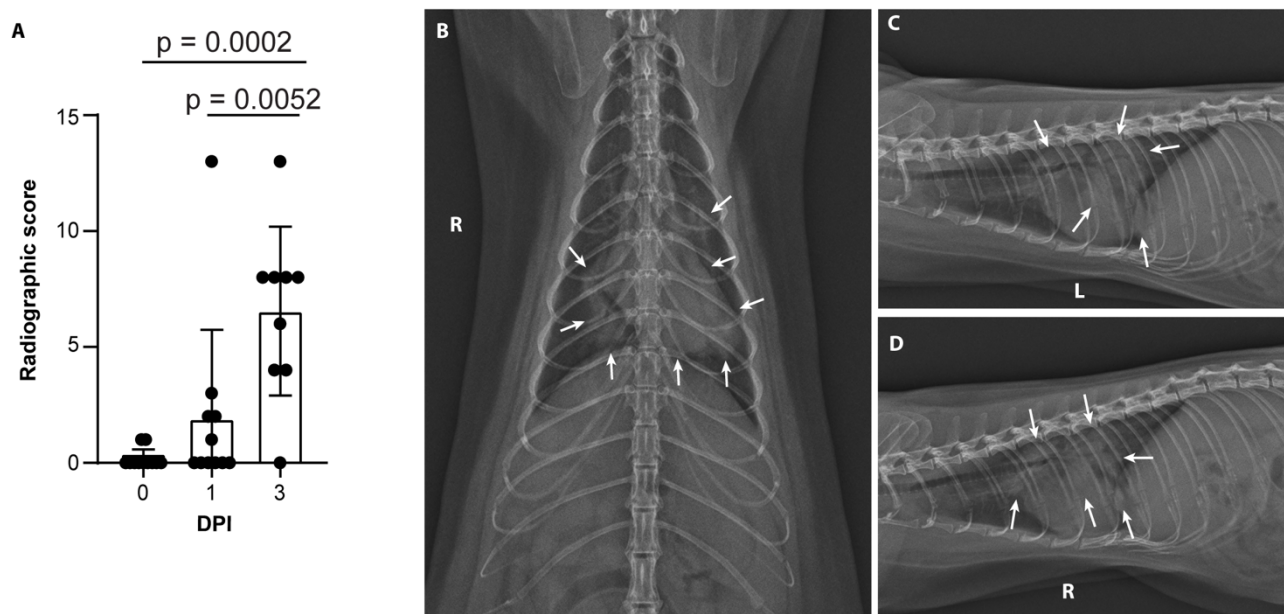


**Figure 3. Severe radiological changes after infection with SARS-CoV-2.** (A) Compiled radiographic scores. Bar graph depicts the mean with standard deviation and individuals, ordinary one-way ANOVA with Tukey's multiple comparisons test. Radiographs demonstrate multifocal pulmonary infiltrates, most severe in the left and right caudal lung lobes depicted in the (B) dorsoventral radiograph (C) left lateral and (D) right lateral radiograph on evening of 2 DPI. Arrows depict grade 4 pulmonary disease in the left and right caudal lung lobes with grade 3 pulmonary disease in the right middle lung lobe and cranial subsegment of the left cranial lung lobe.

157 progression that was characterized  
158 by increased severity and more  
159 extensive distribution of identified  
160 multifocal alveolar pattern (grade  
161 3 to 4).

162 The remaining animal was  
163 monitored for resolution of disease  
164 over 28 days. Changes consistent  
165 with viral pneumonitis were first  
166 detected on 3 DPI, with the most  
167 severe changes noted on 5 DPI  
168 characterized by alveolar pattern in  
169 both caudal lung lobes. These  
170 changes began to resolve on 7 DPI  
171 with complete resolution noted on  
172 14 DPI. (Supplemental Figure 3).

173 **Pathological changes in mink**  
174 **resemble severe human COVID-**  
175 **19 pulmonary damage and**  
176 **coagulopathy**

177 Necropsy of all animals  
178 was performed immediately after  
179 euthanasia. Lung weight to body

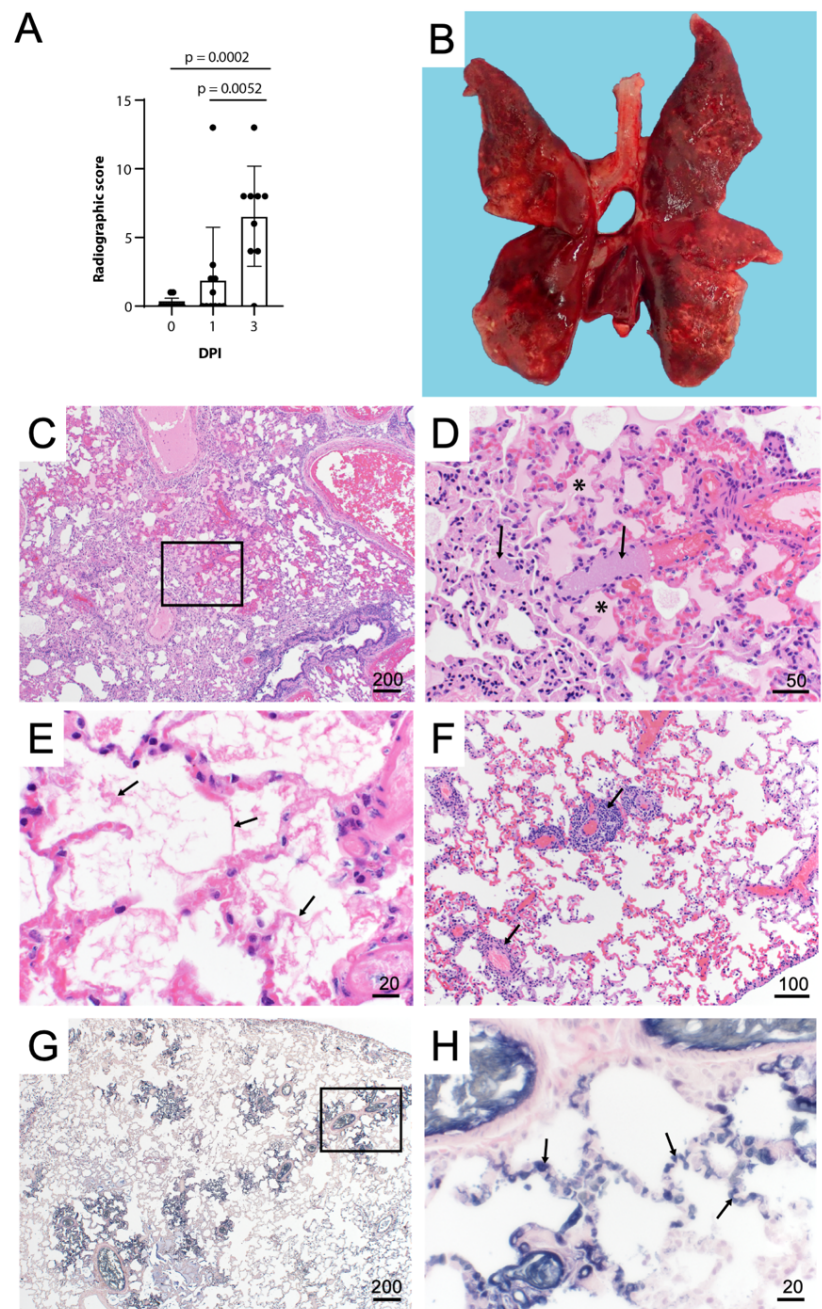


**Figure 4. Pulmonary histopathology and immunohistochemistry.** (A) Lung to body weight ratio, Mann-Whitney test. Graph depicts median with individuals. (B) Diffusely consolidated dark-mottled red lungs (C) Multifocal pulmonary congestion (Box) (D) Enlarged section of image C, vascular thrombi (arrows) alveolar edema (asterisks) (E) Alveolar fibrin (arrows) (F) Lymphoplasmacytic perivascular cuffing (arrows) (G) Pulmonary PTAH staining (black) (H) Enlarged section of image G, microthrombi (arrows). Scale bar expressed in  $\mu\text{m}$  in lower right corner of each image.

180 weight ratio was assessed to estimate the extent of pulmonary edema, and the ratio was  
181 significantly increased in infected animals compared to uninfected controls (Figure 4A). There  
182 were varying degrees of gross pulmonary pathology evident in all 10 animals euthanized on 2 or  
183 3 DPI, with 100% of some lungs affected (Figure 4B). Grossly, lungs were hyperemic, and  
184 several animals had undergone pulmonary hepatization (Figure 4B).

185 Histopathologic lesions associated with SARS-CoV-2 were restricted to the nasal  
186 turbinates and lungs of animals euthanized on 2 or 3 DPI. Nasal turbinates were characterized by  
187 a marked neutrophilic rhinitis with multifocal respiratory epithelial degeneration, necrosis, and  
188 loss. Nasal cavities were filled with an exudate composed of abundant neutrophilic and necrotic  
189 debris. There was rare neutrophilic infiltration of olfactory epithelium (Figure 5). Pulmonary  
190 pathology was more severe in 3 of 10 animals euthanized on 2 or 3 DPI. Lesions consisted of  
191 moderate to marked vascular congestion (Figure 5, C, D) with thickening of the alveolar septa by  
192 edema, fibrin, and cellular infiltrate. Multifocal fibrin thrombi were identified in the vasculature  
193 of regions of congestion (Figure 5, E, F). Alveolar lumina often contained abundant edema fluid,  
194 fibrin, and increased number of alveolar macrophages. There was a moderate lymphoplasmacytic  
195 perivascular cuffing. Bronchial and bronchiolar epithelium was generally unaffected. The  
196 remaining seven animals had mild congestion, moderate lymphoplasmacytic perivascular cuffing  
197 with a mild increase in alveolar macrophages. SARS-CoV-2 antigen was observed  
198 predominately in pulmonary macrophages, although it was unclear if this was the result of  
199 replication or phagocytosis of viral antigen (Supplemental Figure 4, A, B). Multifocal SARS-  
200 CoV-2 antigen positivity was identified in bronchial epithelium and type I and II pneumocytes  
201 and bronchiolar epithelium (Supplemental Figure 5, C, D).

202 **Viral shedding is**  
203 **detected as early as**  
204 **1 DPI in**  
205 **experimentally**  
206 **infected mink**

207       Viral RNA  
208 was detected from  
209 all animals  
210 beginning on 1 DPI,  
211 with the highest viral  
212 RNA loads detected  
213 in oral and nasal  
214 swabs. In nasal, oral,  
215 and rectal swabs,  
216 both genomic  
217 (gRNA) RNA and  
218 sub-genomic RNA  
219 (sgRNA) were  
220 detected, with  
221 sgRNA as a marker

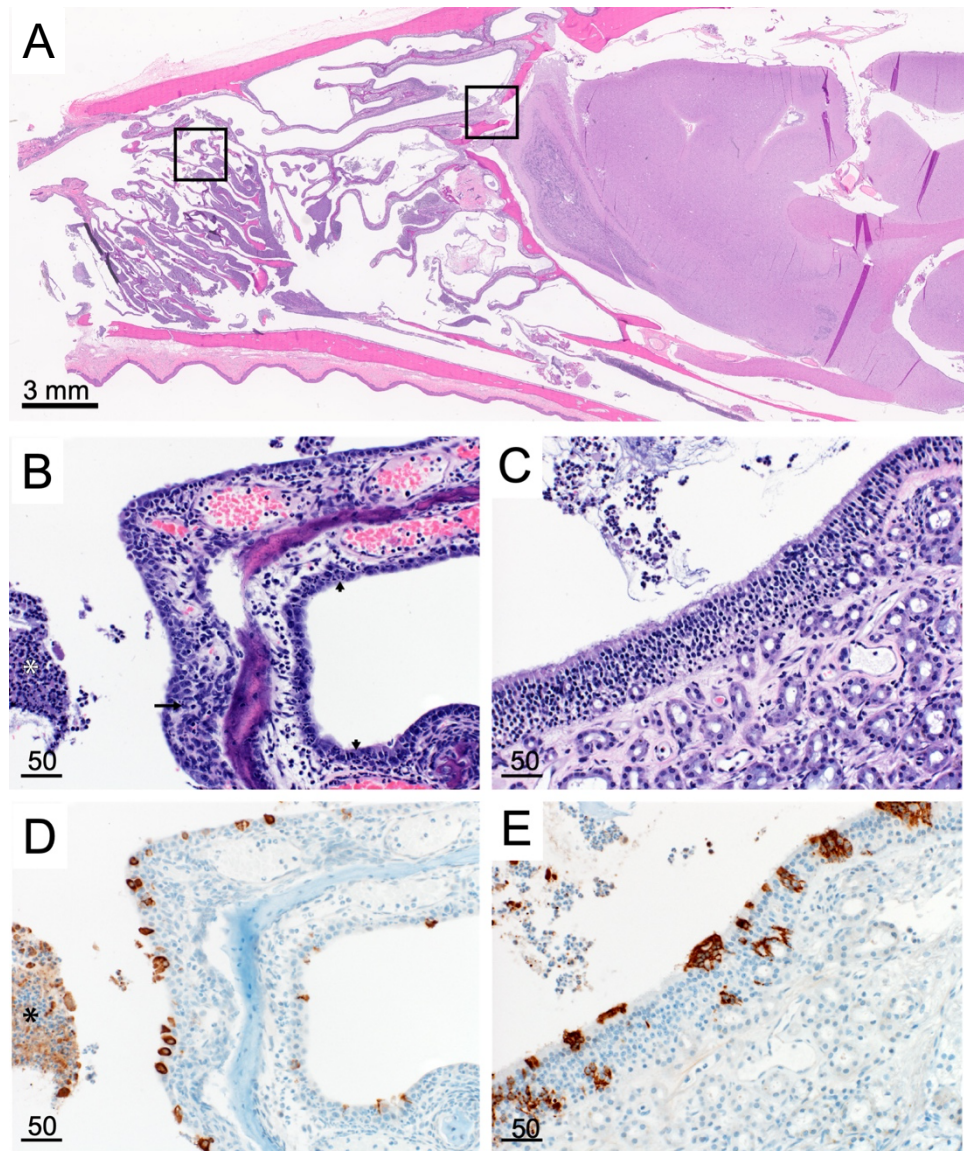


**Figure 5. Nasal turbinate pathology and histopathology.** (A) Sagittal section of skull, H&E (B) Respiratory epithelium neutrophilic infiltrates (small arrows) necrotic epithelium (long arrow) cellular exudate (asterisk) (C) Olfactory epithelium with cellular exudate (D) Respiratory epithelium SARS-CoV-2 IHC immunoreactivity (brown), immunoreactive cellular exudate (asterisk) (E) Olfactory epithelium SARS-CoV-2 IHC immunoreactivity and cellular exudate (brown). Scale bars expressed in  $\mu\text{m}$  unless indicated.

222 for viral replication. Viral RNA was readily detected in both oral and nasal swabs (Figure 6, A,  
223 B). Viral RNA was also detected in rectal swabs collected from 4 of 11 (36 %) animals at 1 DPI  
224 and 3 of 9 (33%) animals at 3 DPI. (Figure 6C). Fur swabs were collected to estimate the risk of

225 handlers and  
 226 processors in the  
 227 fur industry;  
 228 genomic RNA  
 229 was detected  
 230 from most  
 231 animals (Figure  
 232 4D). In the sole  
 233 animal that  
 234 survived until 28  
 235 DPI, viral RNA  
 236 was detected in  
 237 nasal swabs until  
 238 7 DPI and oral  
 239 swabs until 10  
 240 DPI  
 241 (Supplemental  
 242 Figure 2C).  
 243  
 244 Infectious virus was detected in most oral and nasal swabs at 1 (8 of 9, 89%) and 3 (7 of  
 245 8; 88%) DPI. Low amounts of infectious virus were detected in one rectal swab on 1 DPI (1.5  
 246 log<sub>10</sub> TCID<sub>50</sub>/ml) and one fur swab on 3 DPI (0.75 log<sub>10</sub> TCID<sub>50</sub>/ml). Infectious virus was  
 247 detected in the surviving animal until 7 DPI in nasal swabs, and 10 DPI in oral swabs (Figure 6,  
 A, B).

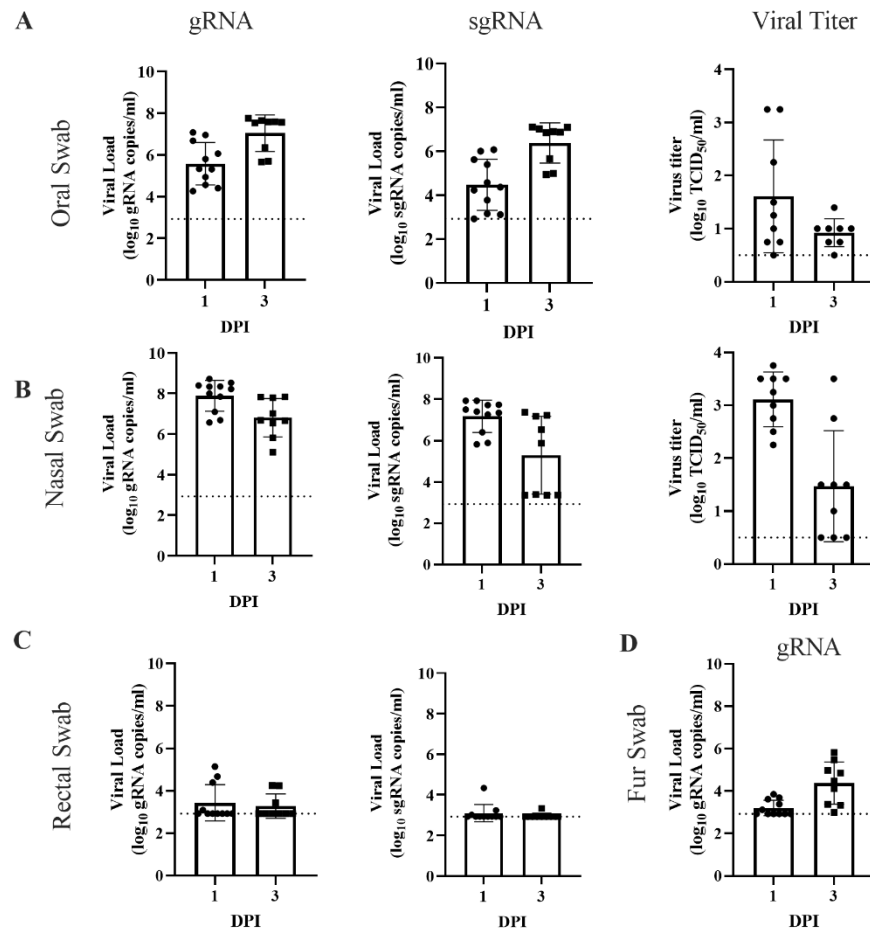


**Figure 6. Viral shedding in infected mink.** Oral (A), nasal (B), rectal (C), and fur (D) swabs were collected on 1 and 3 DPI and analyzed for genomic RNA, sub-genomic RNA, and infectious virus. Bar graphs depict the mean and standard deviation and individuals. Dotted line indicates the limit of detection.

## 248 High viral load in respiratory tract of SARS-CoV-2-infected mink

249 At

250 necropsy, 37

251 tissues were

252 collected from

253 each animal and

254 analyzed for the

255 presence of both

256 gRNA and

257 sgRNA. gRNA

258 and sgRNA was

259 detected in the

260 tissues from all

261 animals

262 necropsied on 2

263 or 3 DPI (Figure

264 7, Supplemental

265 Figure 6). While

266 viral RNA was

267 detected in multiple organ systems, the highest viral loads were detected in respiratory tissues

268 (Figure 7A, B). Within the respiratory tract, the highest viral loads were detected in the upper

269 (nasal turbinate) and lower (all lung lobes) as compared to the mid-respiratory tract (trachea,

270 right and left bronchus). In addition, high levels of viral RNA were detected in the frontal lobe,

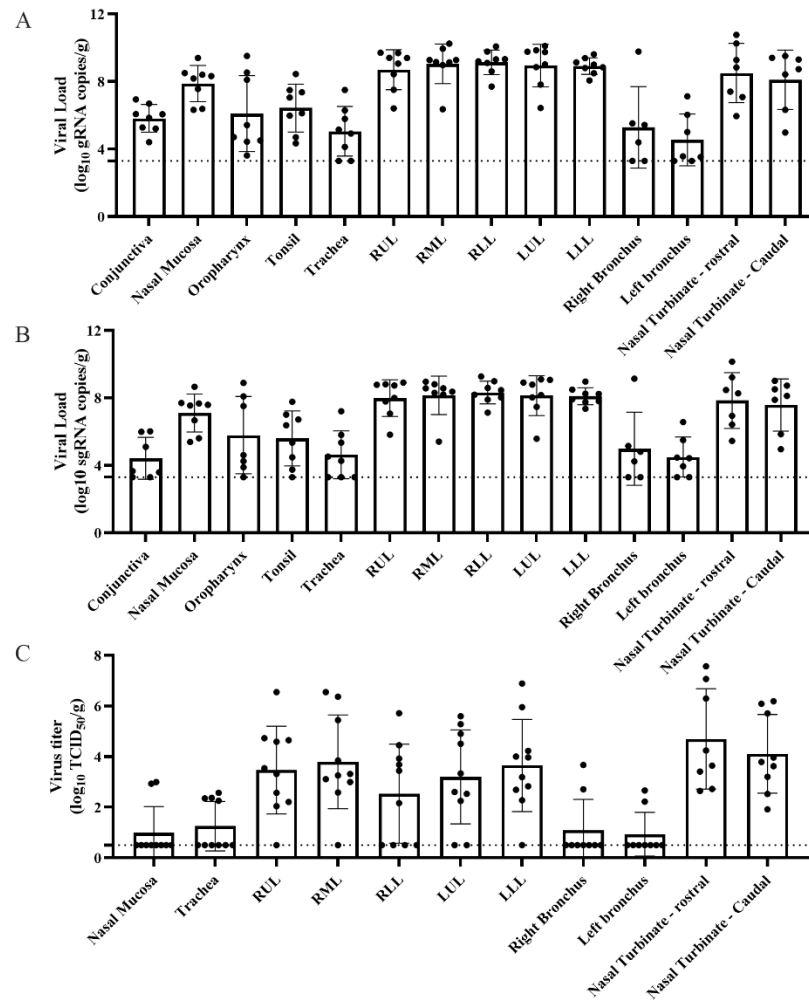


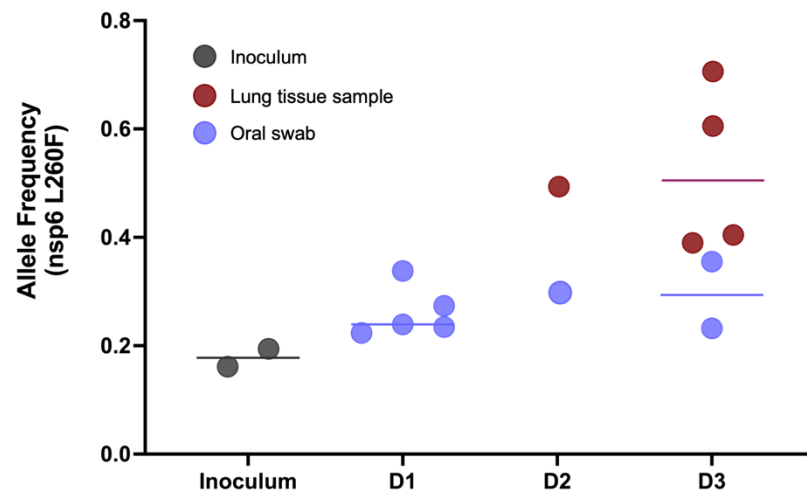
**Figure 7. High levels of viral replication in the respiratory tract of infected mink.** Tissues from animal euthanized on 3 DPI were analyzed for genomic (A), sub-genomic (B), and infectious virus (C). Bar graphs depict individuals, mean, and standard deviation. The dotted line depicts the limit of detection.

271 cerebellum, and brainstem (Supplemental Figure 6). Despite high levels of viral RNA, SARS-  
272 CoV-2 antigen was not observed in the olfactory bulb, cerebral cortex, or brainstem  
273 (Supplemental Figure 5). The respiratory tract was tested for the presence of infectious virus,  
274 with the majority of infectious virus found in the upper and lower respiratory tract (Figure 7C).

### 275 **Within-host evolution of SARS-CoV-2 in mink indicates potential for rapid adaptation**

276 SARS-CoV-2 genomes were deep sequenced for 23 oral swabs and 10 lung tissue  
277 samples and the SARS-CoV-2 inoculum diluent used in the experimental challenge  
278 (Supplemental Table 1). The deep sequencing runs yielded an average of 88,686 reads mapped  
279 for each sample (Supplemental Table 1). One sample for which fewer than 50,000 reads were  
280 recovered was not used in

281 subsequent analyses. Direct  
282 comparison of intrahost  
283 single nucleotide variants  
284 (iSNVs) detected at minor  
285 allele frequency thresholds of  
286 3% and 5% showed a lack of  
287 concordance between



288 technical replicates  
289 (Supplemental Figure 7),  
290 regardless of the SARS-CoV-  
291 2 genome copy number  
292 (Supplemental Figure 8A) or  
293 the number of sequencing

**Figure 8. Enrichment of a nonsynonymous mutation (L260F) in the gene encoding for *nonstructural protein 6* in ORF1a of SARS-CoV-2 in oral swabs and lung tissue samples of five experimentally challenged mink.** Deep sequencing of SARS-CoV-2 positive samples show rapid enrichment for L260F in *nsp6* in lung tissue samples but not the oral swabs for five of ten experimentally inoculated mink with SARS-CoV-2 genomic material detected in the lungs. Oral swab samples indicated by blue and lung tissue samples indicated by red, the line indicates group mean. Allele frequency for the L260F mutation is plotted on the y-axis.

294 reads mapped for the sample (Supplemental 8B). These results are consistent with findings in  
295 other deep viral genome sequencing efforts (19, 20) and the need for tempered conclusions with  
296 the detection of low-level variants and small datasets. Therefore, we focus on changes in  
297 consensus sequence relative to the inoculum. Consensus sequences were largely unchanged from  
298 the SARS-CoV-2 inoculum sequence in all samples with the exception of a nonsynonymous  
299 mutation in the gene encoding nonstructural protein 6 (*nsp6*, L260F) which appeared enriched in  
300 the lung tissue samples of 5 mink relative to the inoculum and the oral swab samples (Figure 8).  
301 This mutation was identified eight times in 1064 available mink-associated SARS-CoV-2  
302 genome sequences recovered from GISAID including a farmed mink in the USA  
303 (EPI\_ISL\_1014945) in Oct 2020, three mink the Netherlands (EPI\_ISL\_523102, 577749, and  
304 523102) in May and Aug 2020, and four mink in Latvia (EPI\_ISL\_8514994, 8514995, 8514997,  
305 and 4548647, Supplemental Table 2) in July and Sept 2021.

### 306 **Seroconversion in surviving mink by 14 DPI**

307 We analyzed serum for the development of a neutralizing antibody response. All animals  
308 had a titer of <20 prior to challenge and only the surviving animal developed a measurable  
309 neutralizing response. This animal seroconverted by 14 DPI with a peak neutralizing titer of 960,  
310 which decreased to a titer of 640 at euthanasia at 28 DPI.

### 311 **DISCUSSION**

312 The continued emergence of SARS-CoV-2 variants of interest and variants of concern  
313 highlight the urgent need for animal models who consistently recapitulate the spectrum of  
314 disease in COVID-19 patients. Overall, the pseudotype entry data from this study demonstrates  
315 comparable spike entry between human and mink ACE2 confirming the suitability of mink for  
316 modeling SARS-CoV-2 infection and COVID-19 diseases.



317 Humans infected with SARS-CoV-2 present with a spectrum of clinical disease that  
318 ranges from asymptomatic infection to severe disease characterized by respiratory distress,  
319 sepsis, or multiorgan failure. Currently, an animal model for severe COVID-19 disease is not  
320 available (1). Most human infections are confined to the upper respiratory tract. Mild or early  
321 disease manifests with nonspecific symptoms that can include fatigue, fever, headache, loss of  
322 smell and taste, congestion, and fever (21). Progression into severe disease is typically presented  
323 as worsening respiratory disease, hypoxemia, and radiographic lesions, with end-point markers  
324 that can include coagulopathies, thromboembolism, acute kidney injury, and ARDS (21-24).  
325 Infected mink displayed clinical disease consistent with worsening human COVID-19 disease.  
326 Infected mink consistently demonstrated a greater degree of weight loss than that reported in  
327 nonhuman primates or hamsters in the days following infection. Increased respiratory effort and  
328 tachypnea in mink mark progression into severe COVID-19 disease. This study did not look at  
329 odor discrimination; however, neutrophilic infiltrate in olfactory epithelium could suggest a loss  
330 of smell that resulted in decreased appetite. Interestingly, while multiple field reports of fur farm  
331 outbreaks commonly report nasal discharge, this was not a consistent finding in these mink.

332 Features of complete blood counts of COVID-19 disease patients include leukopenia,  
333 lymphopenia, thrombocytopenia, and an increased NLR (13,21,25,26). While we were unable to  
334 rule out a stress leukogram resulting in increased NLR, this finding has been reported in ferrets  
335 infected with H5N1(27) and approximates critically ill human COVID-19 disease patients, where  
336 NLR can be used as a prognostic indicator (25). Interestingly, the NLR ratio for the single  
337 surviving animal was highest on 5 DPI, when the most severe changes were observed on thoracic  
338 radiographs. Mink displayed minimal to mild hypoproteinemia and hypoalbuminemia in the face  
339 of clinical dehydration, indicating a true hypoproteinemia. During acute disease, albumin can act

340 as a negative phase protein and hypoalbuminemia has been associated with poor outcomes in  
341 COVID-19 patients (28,29).

342 One important hallmark of severe human COVID-19 disease is progression to ARDS.  
343 The Berlin Definition of ARDS addresses timing, thoracic imaging, the origin of thoracic edema,  
344 and the degree of hypoxemia (23). Our high-dose intratracheal inoculation likely contributed to  
345 the acute presentation of disease, and additional studies are necessary to better understand the  
346 course of SARS-CoV-2 infection in mink in relationship to dose, route of inoculation, and other  
347 emerging variants. Similar to the radiologic features described in humans, mink displayed  
348 bilateral ground glass opacities (30). However, unlike humans, these radiological features were  
349 not most severe in the gravitationally dependent regions (30). One theory explaining this atypical  
350 distribution is that the method of viral inoculation may have resulted in greater distribution in the  
351 caudal lung lobes as the virus was administered intratracheally in anesthetized subjects as  
352 opposed to a more passive inhalation of viral fomites. Additionally, a component of non-  
353 cardiogenic pulmonary edema, secondary to ARDS, may contribute to pulmonary infiltrates and  
354 is more commonly distributed in the caudal lung lobes. The hearts were radiographically and  
355 grossly normal, indicating the pulmonary changes were not likely due to cardiogenic pulmonary  
356 edema. Finally, this study was not able to evaluate the degree of hypoxemia, a critical step in  
357 diagnosing ARDS (23). Additional studies using advanced tools such as the flexiVent (SCIREQ,  
358 Emka Technologies Co., Sterling, VA, USA) and blood gas analysis are required to fully  
359 evaluate this model for clinical ARDS (2,29,31,32).

360 Histologically, diffuse alveolar disease (DAD) is an important finding in patients with  
361 severe COVID-19 disease and has not been regularly described in currently available animal  
362 models. Although not every mink had severe pulmonary pathology, all 10 animals euthanized on

363 2 or 3 DPI displayed pathology consistent with human COVID-19 disease (24). Animals with  
364 less severe histologic disease likely represent earlier stages in disease progression and follow up  
365 studies are required to better understand disease progression. The multifocal fibrin thrombi,  
366 cellular infiltrate, and resulting edema in the 3 mink with histologically severe disease likely  
367 reflects a coagulopathy, described in human patients with severe disease (29,33). Additional  
368 studies focusing on D-dimer, fibrinogen, and PT/aPTT are required to further tease out the  
369 pathogenesis in this model (29).

370         Outbreaks of COVID-19 on mink farms suggest the potential for novel SARS-CoV-2  
371 variants to emerge in mink, with a high probability of spillback (7-11,17). This study provides  
372 experimental evidence of rapid enrichment in 5 of 10 mink for L260F in the gene encoding for  
373 nonstructural protein 6 in SARS-CoV-2 (Figure 8) which is hypothesized to affect viral  
374 autophagy and suppress the type I interferon response (18,19). This mutation has been identified  
375 in multiple COVID-19 outbreaks on mink farms in the Netherlands, Latvia, and the US.  
376 Interestingly, enrichment for the L260F mutation is most prominent in the lung tissue samples  
377 rather than the oral swabs, suggesting some tissue-specific tropism and likely a reduced  
378 probability of onward transmission. The repeated detection of the L260F mutation among  
379 COVID-19 outbreaks on mink farms through time and space supports that this mutation confers  
380 a selective advantage in mink and merits further study.

381         A pre-clinical model of severe COVID-19 disease is desperately needed to better evaluate  
382 SARS-CoV-2 vaccines and therapeutics. Current models demonstrate a reduction in viral titer  
383 and reduction of mild pathology, but no current model can recapitulate severe disease. In this  
384 study, we showed the utility of experimentally infected mink as a model for severe human  
385 COVID-19 disease. After infection, mink develop severe clinical disease associated with

386 histological changes consistent with worsening human disease, making this new model the most  
387 translatable animal model available for severe COVID-19 disease.

## 388 **Materials and Methods**

### 389 *Experimental Design*

390 The objective of this study is to evaluate American mink as an animal model of severe  
391 COVID-19. SARS-CoV-2 infection in the American mink were determined through virological,  
392 histopathological, clinical, and radiographical analyses. Comparative analyses of functional  
393 SARS-CoV-2 entry using human and mink ACE2 were determined through a vesicular stomatitis  
394 virus pseudotyping assay. Deep viral genome sequencing was employed to study the intrahost  
395 evolutionary dynamics in the experimentally infected mink.

### 396 *Ethics statement*

397 All animal experiments were approved by the Institutional Animal Care and Use  
398 Committee of Rocky Mountain Laboratories, NIH and carried out in an Association for  
399 Assessment and Accreditation of Laboratory Animal Care (AALAC) International accredited  
400 facility, according to the institution's guidelines for animal use, following the guidelines and  
401 basic principles in the Guide for the Care and Use of Laboratory Animals, the Animal Welfare  
402 Act, United States Department of Agriculture and the United States Public Health Service Policy  
403 on Humane Care and Use of Laboratory Animals. The Institutional Biosafety Committee (IBC)  
404 approved work with infectious SARS-CoV-2 strains under BSL3 conditions. Sample inactivation  
405 was performed according to IBC-approved standard operating procedures for removal of  
406 specimens from high containment.

### 407 *Mink ACE2 Sequence and modeling*

408 DNA was extracted from mink lung tissue using QIAamp DNA Tissue Kit according to  
409 the manufacturer. Mink ACE2 full length gene was amplified using long range PCR (LRPCR)  
410 amplification assay in two overlapping fragments using high-fidelity PrimeSTAR GXL DNA  
411 Polymerase (Takara Bio USA) as previously described (34,35). Briefly, 50  $\mu$ L LRPCR master  
412 mix contained 0.2  $\mu$ M of each primer (Supplementary Table 3), 1X PrimeSTAR GXL Buffer,  
413 200  $\mu$ M each deoxyribonucleotide triphosphate, 5  $\mu$ L cDNA template, and 1.25 units of  
414 PrimeSTAR GXL DNA Polymerase (Takara Bio USA, Inc., San Jose, CA). The LRPCR mixture  
415 was incubated at 98°C for 2 minutes for the initial denaturation, followed by 4 cycles at 98°C for  
416 10 seconds, 68°C for 15 seconds ( $-2^\circ\text{C}$  per cycle), and 72°C for 10 minutes before an additional  
417 26 cycles of 98°C for 10 seconds, 56°C for 15 seconds, and 72°C for 10 minutes. Sequencing  
418 libraries were generated using the TruSeq DNA PCR-Free library prep kit (Illumina Inc., San  
419 Diego, CA, USA) and sequenced on an Illumina MiSeq instrument at 2 x 151 paired-end reads.  
420 Reads were *de novo* assembled using SPAdes v. 3.13 (36). Sequence alignments between  
421 American mink (*Neovison vison*, sequence generated in this study) ACE2, European mink ACE2  
422 (*Mustela lutreola biedermanni*, GenBank QNC68911.1), and human ACE2 (*Homo sapiens*,  
423 GenBank BAB40370.1) were generated using Multalin (37) and plotted using ESPript (38).  
424 Residues that participate in the SARS-CoV-2 RBD–ACE2 interaction, as described by Lan et al.  
425 (17), are noted below the alignment. The percent identity between the ACE2 sequences was  
426 calculated by Clustal Omega (39).

427 Structure analysis utilized the human ACE2 and SARS-CoV-2 RBD crystal structure,  
428 PDB ID 6M0J (17). Mutagenesis to show residues that differ in mink ACE2, and the alpha and  
429 delta variant RBD, was performed in COOT (40). The figures were generated using The Pymol  
430 Molecular Graphics System (<https://www.schrodinger.com/pymol>).

431 *Plasmids*

432           The spike coding sequences for SARS-CoV-2 lineage B (hCoV-19/Denmark/DCGC-  
433 3024/2020, EPI\_ISL\_616802) were truncated by deleting 19 aa at the C-terminus. The S proteins  
434 with the 19 AA deletion of coronaviruses were previously reported to show increased efficiency  
435 regarding incorporation into virions of VSV (41,42). These sequences were codon optimized for  
436 human cells, then appended with a 5' kozak expression sequence (GCCACC) and 3' tetra-glycine  
437 linker followed by nucleotides encoding a FLAG-tag sequence (DYKDDDDK). These spike  
438 sequences were synthesized and cloned into pcDNA3.1<sup>+</sup> (GenScript Biotech, Piscataway, NJ,  
439 USA). Mink ACE2 were synthesized and cloned into pcDNA3.1<sup>+</sup> (GenScript Biotech,  
440 Piscataway, NJ, USA). All DNA constructs were verified by Sanger sequencing (ACGT).

441 *Pseudotype production and luciferase-based cell entry assay*

442           Pseudotype production was carried out as described previously (16). Briefly, plates pre-  
443 coated with poly-L-lysine (Sigma-Aldrich, St. Louis, MO, USA) were seeded with 293T cells  
444 and transfected the following day with 1,200 ng of empty plasmid and 400 ng of plasmid  
445 encoding coronavirus spike or no-spike plasmid control (green fluorescent protein (GFP)). BHK  
446 cells were seeded in black 96-well plates and transfected the next day with 100 ng plasmid DNA  
447 encoding human or mink ACE2, using polyethylenimine (Polysciences, Inc., Warrington, PA,  
448 USA). After 24 hours, transfected cells were infected with VSV $\Delta$ G seed particles pseudotyped  
449 with VSV-G, as previously described (16,43). After one hour of incubating with intermittent  
450 shaking at 37 °C, cells were washed four times and incubated in 2mL DMEM supplemented with  
451 2% fetal bovine serum (FBS), penicillin/streptomycin and L-glutamine for 48 hours.  
452 Supernatants were collected, centrifuged at 500xg for 5 minutes, aliquoted, and stored at -80 °C.  
453 BHK cells previously transfected with ACE2 plasmid of interest were inoculated with equivalent

454 volumes of pseudotype stocks. Plates were then centrifuged at 1200xg at 4 °C for one hour and  
455 incubated overnight at 37 °C. Approximately 18-20 hours post-infection, Bright-Glo luciferase  
456 reagent (Promega Corp., Madison, WI, USA) was added to each well, 1:1, and luciferase was  
457 measured. Relative entry was calculated normalizing the relative light unit for each pseudotyped  
458 spike to the relative light unit average for the no-spike control.

#### 459 *Animals*

460         Seventeen apparently healthy adult farmed mink (*Neovison vison*) were used in this  
461 study: 11 were used for experimental infection and 6 were used as controls. All mink were pre-  
462 screened and negative for SARS-CoV-2 using a qRT-PCR, a pan-coronavirus assay (44), viral  
463 neutralization assay, and Aleutian disease using a lateral flow immunoassay (Scintilla  
464 Development Company LLC, Bath, Pennsylvania).

465 The animals used in the infection study consisted of 9 females and two males; intake female  
466 body weight range 1.04 kg – 1.47 kg, mean = 1.18 kg, male weights were 2.06 kg and 2.73. The  
467 females were approximately two years of age, the males were approximately one year of age.

468 Upon arrival whole blood from all mink were screened for antibodies against SARS-CoV-2.

469 Animals were single-housed in a climate-controlled room with a fixed light-dark cycle (12-hour  
470 light and 12-hour dark) for the duration of the experiment with access to food and water *ad*

471 *libitum* with enrichment that included human interaction, commercial toys, music, and treats. All

472 manipulations were done on anesthetized animals using Telazol (10-20 mg/kg administered

473 subcutaneously).

#### 474 *Animal study*

475         Eleven animals were inoculated intratracheally (1.7 mL) and intranasally (0.15 mL per  
476 naris delivered using a MAD Nasal™ Mucosal Atomization Device (Teleflex, US) for a total

477 dose of  $10^5$  TCID<sub>50</sub> delivered in 2 total mL. Animals were evaluated at least twice daily  
478 throughout the study. Clinical exams (including thoracic radiographs) were performed on 0, 1, 3,  
479 5, 7, 10, 14, 17, 21, 28 DPI on anesthetized animals, during which the following parameters were  
480 assessed: bodyweight, body temperature, heart rate, respiratory rate, and radiographs. Clinical  
481 samples collected included nasal, oral, rectal, and fur swabs, and blood. Fur swabs were  
482 collected down the dorsal midline of the animal. Swabs were collected in 1mL of DMEM  
483 supplemented with 2% FBS, 1 mM L-glutamine, 50 U/ml penicillin, and 50 g/ml streptomycin.

#### 484 *Radiographs*

485 Ventrodorsal, left lateral, and right lateral thoracic radiographs were taken prior to  
486 clinical exams on 0, 1, 3, 5, 7, 10, 14, 17, 21, and 28 DPI with 0 DPI being performed prior to  
487 inoculation and serving as a baseline. Thoracic radiographs were taken immediately after  
488 animals were anesthetized and each lung lobe was evaluated by a board-certified veterinary  
489 radiologist as follows: 0 = normal lung, 1 = mild interstitial infiltrate, 2 = moderate to marked  
490 unstructured interstitial pattern, 3 = <25% alveolar pattern, 4 = >25% alveolar pattern.

#### 491 *Clinical pathology*

492 Hematology analysis was completed on a ProCyte Dx® (IDEXX Laboratories,  
493 Westbrook, ME, USA) and the following parameters were evaluated: red blood cells (RBC);  
494 hemoglobin (Hb); hematocrit (HCT); mean corpuscular volume (MCV); mean corpuscular  
495 hemoglobin (MCH); mean corpuscular hemoglobin concentration (MCHC); red cell distribution  
496 width (RDW); platelets; mean platelet volume (MPV); white blood cells (WBC); neutrophil  
497 count (absolute and percentage); lymphocyte count (absolute and percentage); monocyte count  
498 (absolute and percentage); eosinophil count (absolute and percentage); and basophil count  
499 (absolute and percentage). Serum chemistry analysis was completed on a VetScan VS2®



500 Chemistry Analyzer (Abaxis, Union City CA) and the following parameters were evaluated:  
501 glucose; blood urea nitrogen (BUN); creatinine; calcium; albumin; total protein; alanine  
502 aminotransferase (ALT); aspartate aminotransferase (AST); alkaline phosphatase (ALP); total  
503 bilirubin; globulin; sodium; potassium; chloride and total carbon dioxide. Clinical pathology  
504 samples were evaluated by a board-certified clinical veterinarian.

#### 505 *Histopathology*

506 Histopathology and immunohistochemistry were performed on mink tissues. Tissues  
507 were fixed for a minimum of 7 days in 10% neutral-buffered formalin with 2 changes. Tissues  
508 were placed in cassettes and processed with a Sakura VIP-6 Tissue Tek, on a 12-hour automated  
509 schedule, using a graded series of ethanol, xylene, and PureAffin. Embedded tissues were  
510 sectioned at 5um and dried overnight at 42 degrees C prior to staining. The skulls were placed in  
511 Cancer Diagnostic acid free EDTA for 4 weeks and the solution was changed weekly.

512 Tissue sections were stained with hematoxylin and eosin (HE). The tissues were then  
513 processed for immunohistochemistry using the Discovery Ultra automated stainer (Roche  
514 Tissues Diagnostics) with a ChromoMap DAB kit (Roche Tissue Diagnostics cat #760-159).  
515 Specific anti-CoV immunoreactivity was detected using SARS-CoV-2 nucleocapsid antibody  
516 (GenScript Biotech, Piscataway, NJ, USA) at a 1:1000 dilution. The secondary antibody was the  
517 Vector Laboratories ImPress VR anti-rabbit IgG polymer (cat# MP-6401). To detect ACE-2,  
518 ACE-2 Antibody R&D Systems (catalog #AF933) was used at a 1:100 dilution with Vector  
519 Laboratories ImPress anti-goat IgG polymer (Cat #MP-7405) as a secondary antibody.

#### 520 *Virus and cells*

521 SARS-CoV-2 variant B.1.1.7 (hCoV-19/England/204820464/2020, EPI\_ISL\_683466;  
522 designated B.1.1.7 through the manuscript) was obtained from Public Health Agency England

523 via BEI Resources. The obtained passage 2 material was propagated once in VeroE6 cells in  
524 DMEM supplemented with 2% FBS, 1mM L-glutamine, 50 U/ml penicillin, and 50 g/ml  
525 streptomycin. Mycoplasma testing was performed at regular intervals and no mycoplasma was  
526 detected. For sequencing from viral stocks, sequencing libraries were prepared using Stranded  
527 Total RNA Prep Ligation with Ribo-Zero Plus kit per manufacturer's protocol (Illumina Inc.,  
528 San Diego, CA, USA) and sequenced on an Illumina MiSeq at 2 x 150 base pair reads. Low level  
529 sequence variation in the stock of B.1.1.7 (nsp6/D165G/14%, nsp6/L257F/18% and  
530 nsp7/V11L/13%).

#### 531 *RNA extraction and quantitative reverse-transcription polymerase chain reaction*

532 RNA was extracted from nasal, oral, rectal, and fur swabs using the QiaAmp Viral RNA kit  
533 (Qiagen Sciences, Inc., Germantown, MD, USA) according to the manufacturer's instructions  
534 and following high containment laboratory protocols. Tissue samples were homogenized and  
535 extracted using the RNeasy kit (Qiagen Sciences, Inc., Germantown, MD, USA) according to the  
536 manufacturer's instructions and following high containment laboratory protocols. A viral sgRNA  
537 specific assay was used for the detection of viral RNA (46). Five  $\mu$ L of extracted RNA was  
538 tested with the Quantstudio 3 system (Thermofisher Scientific, Waltham, MA, USA) according  
539 to instructions from the manufacturer. A standard curve was generated during each run using  
540 SARS-CoV-2 standards containing a known number of genome copies.

#### 541 *Viral titration*

542 Tissue sections were weighed and homogenized in 1mL of DMEM. Virus titrations were  
543 performed by end point titration of 10-fold dilutions of swab media or tissue homogenates on  
544 VeroE6 cells in 96-well plates. When titrating tissue homogenate, the top 3 rows of cells were

545 washed 2 times with DMEM prior to the addition of a final 100 $\mu$ L of DMEM. Cells were  
546 incubated at 37°C and 5% CO<sub>2</sub>. Cytopathic effect was read 6 days later.

547 *SARS-CoV-2 genome sequencing and within-host evolution*

548 Oral swabs and lung tissue samples were collected into Trizol for RNA extraction. 200  
549  $\mu$ L of 1-Bromo-3-chloropropane (MilliporeSigma, St. Louis, MO, USA) was added to the  
550 Trizol/sample lysate, mixed, and centrifuged at 16,000 x g for 15 min at 4°C. RNA containing  
551 aqueous phase of 600  $\mu$ l was collected from each sample and aqueous phase was combined with  
552 600 $\mu$ L of RLT lysis buffer (Qiagen, Valencia, CA, USA) with 1% beta mercaptoethanol  
553 (MilliporeSigma, St. Louis, MO, USA). RNA was extracted using Qiagen AllPrep DNA/RNA  
554 96-well system (Valencia, CA, USA). An additional on-column Dnase 1 treatment was  
555 performed during RNA extraction. All sample processing was performed using amplicon-free  
556 reagents and tools in aerosol resistant vials. RNA quality was analyzed using Agilent 2100  
557 Bioanalyzer (Agilent Technologies, Santa Clara, CA, USA). RNA samples were quantitated by  
558 qRT-PCR targeting NSP5 using the AgPath-ID One-Step RT-PCR Buffer and Enzyme Mix (Life  
559 Technologies, Carlsbad, CA, USA). The reactions were carried out in 20  $\mu$ L reactions using  
560 NSP5 forward primer (5'-CTGGCACAGACTTAGAAGGTAAGT-3'), reverse primer  
561 (5'TCGATTGAGAAACCACCTGTCT-3'), fluorescent probe (5'-6FAM-  
562 TTGACAGGCAAACAGCACAAGCAG-BHQ1-3') (Biosearch Technologies, Novato, CA,  
563 USA). The QPCR reactions were carried out at 50 °C for 10 minutes, 95 °C for 10 minutes, 55  
564 cycles of 95 °C for 15 seconds and 60 °C for 45 seconds. Data was analyzed using ABI 7900HT  
565 version 2.4 sequence detection system software (Thermofisher Scientific, Waltham, MA, USA)  
566 and SARS-CoV-2 genome copy (equivalent/mL) numbers were determined by absolute  
567 quantitation method. Next generation libraries were generated using the TruSeq DNA PCR Free

568 Nano kit (Illumina, Inc., San Diego, CA, USA) and the ARTIC multiplex PCR genome  
569 amplification protocol with the V3 primer scheme ([www.protocols.io/view/ncov-2019-  
570 sequencing-protocol-bbmuik6w](http://www.protocols.io/view/ncov-2019-sequencing-protocol-bbmuik6w)) and libraries were sequenced on an Illumina MiSeq at 2 x 250  
571 paired-end reads. The ARTIC multiplex PCR SARS-CoV-2 genome amplification protocol has  
572 been widely used in viral genome sequencing during the COVID-19 pandemic and to study  
573 within-host dynamics of SARS-CoV-2 (21).

574 To determine reproducibility of our assay, a subset of 12 samples determined to have  
575 high ( $10^4$ ), medium ( $10^3$ ), and low ( $10^2$ ) SARS-CoV-2 genome copy (equivalent/mL) numbers  
576 by NSP5 qRT-PCR were selected as technical replicates. ARTIC primers and Illumina adapters  
577 were trimmed, low quality bases and duplicate reads were filtered out, and mapping and variant  
578 calling were completed as described in the iVar and PrimalSeq pipeline described by Grubaugh  
579 *et al.*(47). Intrahost single nucleotide variants (iSNVs) were included in further analysis if they  
580 passed the Fisher's exact test for variation above the mean error rate at that locus and had a depth  
581 of coverage at or above 100X. iSNVs were called with minor allele frequency (MAF) thresholds  
582 at 3% and 5% and compared against technical replicates (Supplemental SNS2). iSNVs detected  
583 at 3% MAF were plotted against the SARS-CoV-2 genome copy number for each sample  
584 (Supplemental SNS3A) and the number of reads mapped for each sample (Supplemental  
585 SNS3B).

586 To compare variation arising in the experimentally challenged mink to variation  
587 previously detected in SARS-CoV-2 circulating at mink farms, all available mink-associated  
588 SARS-CoV-2 genomes were downloaded from GISAID from 01-Jan-2020 through 22-Nov-  
589 2021. The resulting alignment of 1002 SARS-CoV-2 genome sequences included 999 with

590 *Neovison vison* as the host species and 3 SARS-CoV-2 sequences from the genus *Mustela*  
591 (GISAID Acknowledgements, Supplemental Table SNS4).

### 592 *Serology*

593 Sera were heat-inactivated (30 min, 56°C). After an initial 1:10 dilution of the sera, two-  
594 fold serial dilutions were prepared in DMEM. 100 TCID<sub>50</sub> of SARS-CoV02 variant B.1.1.7 was  
595 added to the diluted sera. After a 1-hour incubation at 37°C and 5% CO<sub>2</sub>, the virus-serum  
596 mixture was added to VeroE6 cells. The cells were incubated for 6 days at 37°C and 5% CO<sub>2</sub> at  
597 which time they were evaluated for CPE. The virus neutralization titer was expressed at the  
598 reciprocal value of the highest dilution of the serum that still inhibited virus replication.

### 599 *Statistical analysis*

600 Statistical analysis was performed using GraphPad Version 8.4.3. Significance tests were  
601 performed as indicated where appropriate with reported p-values.

602

603 **References**

- 604 1 Muñoz-Fontela, C. *et al.* Animal models for COVID-19. *Nature* **586**, 509-515,  
605 doi:10.1038/s41586-020-2787-6 (2020).
- 606 2 Winkler, E. S. *et al.* SARS-CoV-2 infection of human ACE2-transgenic mice causes  
607 severe lung inflammation and impaired function. *Nat Immunol* **21**, 1327-1335,  
608 doi:10.1038/s41590-020-0778-2 (2020).
- 609 3 Rosenke, K. *et al.* Defining the Syrian hamster as a highly susceptible preclinical model  
610 for SARS-CoV-2 infection. *Emerg Microbes Infect* **9**, 2673-2684,  
611 doi:10.1080/22221751.2020.1858177 (2020).
- 612 4 Shi, J. *et al.* Susceptibility of ferrets, cats, dogs, and other domesticated animals to  
613 SARS-coronavirus 2. *Science (New York, N.Y.)* **368**, 1016-1020,  
614 doi:10.1126/science.abb7015 (2020).
- 615 5 Schlottau, K. *et al.* SARS-CoV-2 in fruit bats, ferrets, pigs, and chickens: an  
616 experimental transmission study. *Lancet Microbe* **1**, e218-e225, doi:10.1016/s2666-  
617 5247(20)30089-6 (2020).
- 618 6 Munster, V. J. *et al.* Respiratory disease in rhesus macaques inoculated with SARS-CoV-  
619 2. *Nature* **585**, 268-272, doi:10.1038/s41586-020-2324-7 (2020).
- 620 7 Richard, M. *et al.* SARS-CoV-2 is transmitted via contact and via the air between ferrets.  
621 *Nat Commun* **11**, 3496, doi:10.1038/s41467-020-17367-2 (2020).
- 622 8 Kutter, J. S. *et al.* SARS-CoV and SARS-CoV-2 are transmitted through the air between  
623 ferrets over more than one meter distance. *Nat Commun* **12**, 1653, doi:10.1038/s41467-  
624 021-21918-6 (2021).

- 625 9 Kim, Y.-I. *et al.* Infection and Rapid Transmission of SARS-CoV-2 in Ferrets. *Cell host*  
626 *& microbe* **27**, 704-709.e702, doi:10.1016/j.chom.2020.03.023 (2020).
- 627 10 Oreshkova, N. *et al.* SARS-CoV-2 infection in farmed minks, the Netherlands, April and  
628 May 2020. *Euro Surveill* **25**, doi:10.2807/1560-7917.Es.2020.25.23.2001005 (2020).
- 629 11 Shriner, S. A. *et al.* SARS-CoV-2 Exposure in Escaped Mink, Utah, USA. *Emerg Infect*  
630 *Dis* **27**, 988-990, doi:10.3201/eid2703.204444 (2021).
- 631 12 Aguiló-Gisbert, J. *et al.* First Description of SARS-CoV-2 Infection in Two Feral  
632 American Mink (*Neovison vison*) Caught in the Wild. *Animals : an open access journal*  
633 *from MDPI* **11**, 1422, doi:10.3390/ani11051422 (2021).
- 634 13 Molenaar, R. J. *et al.* Clinical and Pathological Findings in SARS-CoV-2 Disease  
635 Outbreaks in Farmed Mink (*Neovison vison*). *Vet Pathol* **57**, 653-657,  
636 doi:10.1177/0300985820943535 (2020).
- 637 14 Lassaunière, R. *et al.* *In vitro* characterization of fitness and convalescent antibody  
638 neutralization of SARS-CoV-2 Cluster 5 variant emerging in mink at Danish farms.  
639 *Front Microbiol* **12**:698944, doi: 10.3389/fmicb.2021.698944 (2021).
- 640 15 Enserink, M. Coronavirus rips through Dutch mink farms, triggering culls. *Science* **368**,  
641 1169, doi:10.1126/science.368.6496.1169 (2020).
- 642 16 Letko, M., Marzi, A. & Munster, V. Functional assessment of cell entry and receptor  
643 usage for SARS-CoV-2 and other lineage B betacoronaviruses. *Nature Microbiology* **5**,  
644 562-569, doi:10.1038/s41564-020-0688-y (2020).
- 645 17 Lan, J. *et al.* Structure of the SARS-CoV-2 spike receptor-binding domain bound to the  
646 ACE2 receptor. *Nature* **581**, 215-220, doi:10.1038/s41586-020-2180-5 (2020).

- 647 18 Devaux, C. A. *et al.* Spread of Mink SARS-CoV-2 Variants in Humans: A Model of  
648 Sarbecovirus Interspecies Evolution. *Frontiers in Microbiology* **12**,  
649 doi:10.3389/fmicb.2021.675528 (2021).
- 650 19 Lythgoe, K. A. *et al.* SARS-CoV-2 within-host diversity and transmission. *Science* **372**,  
651 doi:10.1126/science.abg0821 (2021).
- 652 20 Tonkin-Hill, G. *et al.* Patterns of within-host genetic diversity in SARS-CoV-2. *Elife* **10**,  
653 doi:10.7554/eLife.66857 (2021).
- 654 21 Mondello, C. *et al.* Pathological Findings in COVID-19 as a Tool to Define SARS-CoV-  
655 2 Pathogenesis. A Systematic Review. *Frontiers in pharmacology* **12**, 614586-614586,  
656 doi:10.3389/fphar.2021.614586 (2021).
- 657 22 Berlin, D. A., Gulick, R. M. & Martinez, F. J. Severe Covid-19. *N Engl J Med*,  
658 doi:10.1056/NEJMcp2009575 (2020).
- 659 23 Force\*, T. A. D. T. Acute Respiratory Distress Syndrome: The Berlin Definition. *JAMA*  
660 **307**, 2526-2533, doi:10.1001/jama.2012.5669 (2012).
- 661 24 Konopka, K. E. *et al.* Diffuse alveolar damage (DAD) resulting from coronavirus disease  
662 2019 Infection is Morphologically Indistinguishable from Other Causes of DAD.  
663 *Histopathology* **77**, 570-578, doi:10.1111/his.14180 (2020).
- 664 25 Liu, J. *et al.* Neutrophil-to-lymphocyte ratio predicts critical illness patients with 2019  
665 coronavirus disease in the early stage. *Journal of Translational Medicine* **18**, 206,  
666 doi:10.1186/s12967-020-02374-0 (2020).
- 667 26 Liu, Y. *et al.* Neutrophil-to-lymphocyte ratio as an independent risk factor for mortality  
668 in hospitalized patients with COVID-19. *J Infect* **81**, e6-e12,  
669 doi:10.1016/j.jinf.2020.04.002 (2020).



- 670 27 Long, J. P. *et al.* Early indicators of disease in ferrets infected with a high dose of avian  
671 influenza H5N1. *Sci Rep* **2**, 972, doi:10.1038/srep00972 (2012).
- 672 28 Zhang, J. *et al.* Risk factors for disease severity, unimprovement, and mortality in  
673 COVID-19 patients in Wuhan, China. *Clin Microbiol Infect* **26**, 767-772,  
674 doi:10.1016/j.cmi.2020.04.012 (2020).
- 675 29 Salinas, M. *et al.* Laboratory parameters in patients with COVID-19 on first emergency  
676 admission is different in non-survivors: albumin and lactate dehydrogenase as risk  
677 factors. *J Clin Pathol* **74**, 673-675, doi:10.1136/jclinpath-2020-206865 (2021).
- 678 30 Swenson, K. E. & Swenson, E. R. Pathophysiology of Acute Respiratory Distress  
679 Syndrome and COVID-19 Lung Injury. *Critical care clinics* **37**, 749-776,  
680 doi:10.1016/j.ccc.2021.05.003 (2021).
- 681 31 Port, J. R. *et al.* Western diet increases COVID-19 disease severity in the Syrian hamster.  
682 *bioRxiv*, doi:10.1101/2021.06.17.448814 (2021).
- 683 32 Bezuidenhout, M. C. *et al.* Correlating arterial blood gas, acid–base and blood pressure  
684 abnormalities with outcomes in COVID-19 intensive care patients. *Annals of Clinical*  
685 *Biochemistry* **58**, 95-101, doi:10.1177/0004563220972539 (2021).
- 686 33 McGonagle, D., O'Donnell, J. S., Sharif, K., Emery, P. & Bridgewood, C. Immune  
687 mechanisms of pulmonary intravascular coagulopathy in COVID-19 pneumonia. *Lancet*  
688 *Rheumatol* **2**, e437-e445, doi:10.1016/s2665-9913(20)30121-1 (2020).
- 689 34 Seifert, S. N. *et al.* Long-Range Polymerase Chain Reaction Method for Sequencing the  
690 Ebola Virus Genome From Ecological and Clinical Samples. *J Infect Dis* **218**, S301-  
691 S304, doi:10.1093/infdis/jiy290 (2018).

- 692 35 Yinda, C. K. *et al.* A Novel Field-Deployable Method for Sequencing and Analyses of  
693 Henipavirus Genomes From Complex Samples on the MinION Platform. *The Journal of*  
694 *Infectious Diseases* **221**, S383-S388, doi:10.1093/infdis/jiz576 (2019).
- 695 36 Bankevich, A. *et al.* SPAdes: a new genome assembly algorithm and its applications to  
696 single-cell sequencing. *J Comput Biol* **19**, 455-477, doi:10.1089/cmb.2012.0021 (2012).
- 697 37 Corpet, F. Multiple sequence alignment with hierarchical clustering. *Nucleic Acids Res*  
698 **16**, 10881-10890, doi:10.1093/nar/16.22.10881 (1988).
- 699 38 Robert, X. & Gouet, P. Deciphering key features in protein structures with the new  
700 ENDscript server. *Nucleic Acids Res* **42**, W320-324, doi:10.1093/nar/gku316 (2014).
- 701 39 Madeira, F. *et al.* The EMBL-EBI search and sequence analysis tools APIs in 2019.  
702 *Nucleic Acids Research* **47**, W636-W641, doi:10.1093/nar/gkz268 (2019).
- 703 40 Emsley, P., Lohkamp, B., Scott, W. G. & Cowtan, K. Features and development of Coot.  
704 *Acta Crystallogr D Biol Crystallogr* **66**, 486-501, doi:10.1107/s0907444910007493  
705 (2010).
- 706 41 Fukushi, S. *et al.* Vesicular stomatitis virus pseudotyped with severe acute respiratory  
707 syndrome coronavirus spike protein. *J Gen Virol* **86**, 2269-2274,  
708 doi:10.1099/vir.0.80955-0 (2005).
- 709 42 Kawase, M., Shirato, K., Matsuyama, S. & Taguchi, F. Protease-mediated entry via the  
710 endosome of human coronavirus 229E. *J Virol* **83**, 712-721, doi:10.1128/jvi.01933-08  
711 (2009).
- 712 43 Takada, A. *et al.* A system for functional analysis of Ebola virus glycoprotein. *Proc Natl*  
713 *Acad Sci U S A* **94**, 14764-14769, doi:10.1073/pnas.94.26.14764 (1997).

- 714 44 Holbrook, M. G. *et al.* Updated and Validated Pan-Coronavirus PCR Assay to Detect All  
715 Coronavirus Genera. *Viruses* **13**, doi:10.3390/v13040599 (2021).
- 716 45 Rothe, C. *et al.* Transmission of 2019-nCoV Infection from an Asymptomatic Contact in  
717 Germany. *N Engl J Med* **382**, 970-971, doi:10.1056/NEJMc2001468 (2020).
- 718 46 Grubaugh, N. D. *et al.* An amplicon-based sequencing framework for accurately  
719 measuring intrahost virus diversity using PrimalSeq and iVar. *Genome Biol* **20**, 8,  
720 doi:10.1186/s13059-018-1618-7 (2019).

721

722

723

724

725 **Acknowledgements:** We would like to thank Emmie de Wit, Brandi Williamson, Neeltje van  
726 Doremalen, Sujatha Rashid, Ranjan Mukul, Kimberly Stempe, Kent Barbian, and Sarah Anzick  
727 for their assistance with the SARS-CoV-2 isolate. The following reagent was obtained through  
728 BEI Resources, NIAID NIH: Severe Acute Respiratory Syndrome-Related Coronavirus 2, Isolate  
729 hCoV-19/England/204820464/20200, NR-54000, contributed by Bassam Hallis. We are grateful  
730 to Dr. High Hildebrant for providing our Aleution Lateral Flow test. We thank Tina Thomas,  
731 Rebecca Rosenke, and Dan Long for assistance with histology; Brian Smith, Kathy Cordova,  
732 Marissa Woods, Carl Shaia, and Taylor Saturday for technical and data assistance; Anita Mora  
733 for assistance with figures, and Rocky Mountain Veterinary Branch animal care staff for  
734 husbandry. We thank Kimmo Virtaneva and Dan Bruno for their assistance with extractions, the  
735 ARTIC protocol, and sequencing. Stacy Ricklefs assisted with the original isolate sequencing as

736 well as the mink ACE2 sequencing. We also thank Randy Elkins, Steve Denny, and Alphonse Cisar  
737 for additional support.

738

739 **Funding:** This work was supported by the Intramural Research Program of the National Institute  
740 of Allergy and Infectious Diseases (NIAID).

741 The findings and conclusions in this report are those of the authors and do not necessarily  
742 represent the official position of the Centers for Disease Control and Prevention. Use of product  
743 names is for identification purposes only and does not imply endorsement by Centers for Disease  
744 Control and Prevention, the National Institutes of Health, or the U.S. Government.

745

746 **Author contributions:**

747       Conceptualization: DRA, VJM

748       Methodology: DRA, JL, DY, JRS, CT, CC, CE, JE, SNS, VJM

749       Investigation: DRA, JL, JES, VAA, EH, MH, KCY, JRP, SNS, PWH, GS, DS, JVM

750       Visualization: DRA, JL, VAA, PWH, GS, JRS, CT, CC, NMW, SNS

751       Formal analysis: DRA, JL, DY, VAA, SNS, CM

752       Funding acquisition: VJM

753       Resources: JE

754       Supervision: VJM

755       Writing – Original Draft: DRA

756       Writing – Review and editing: DRA, SNS, JRS, VJM

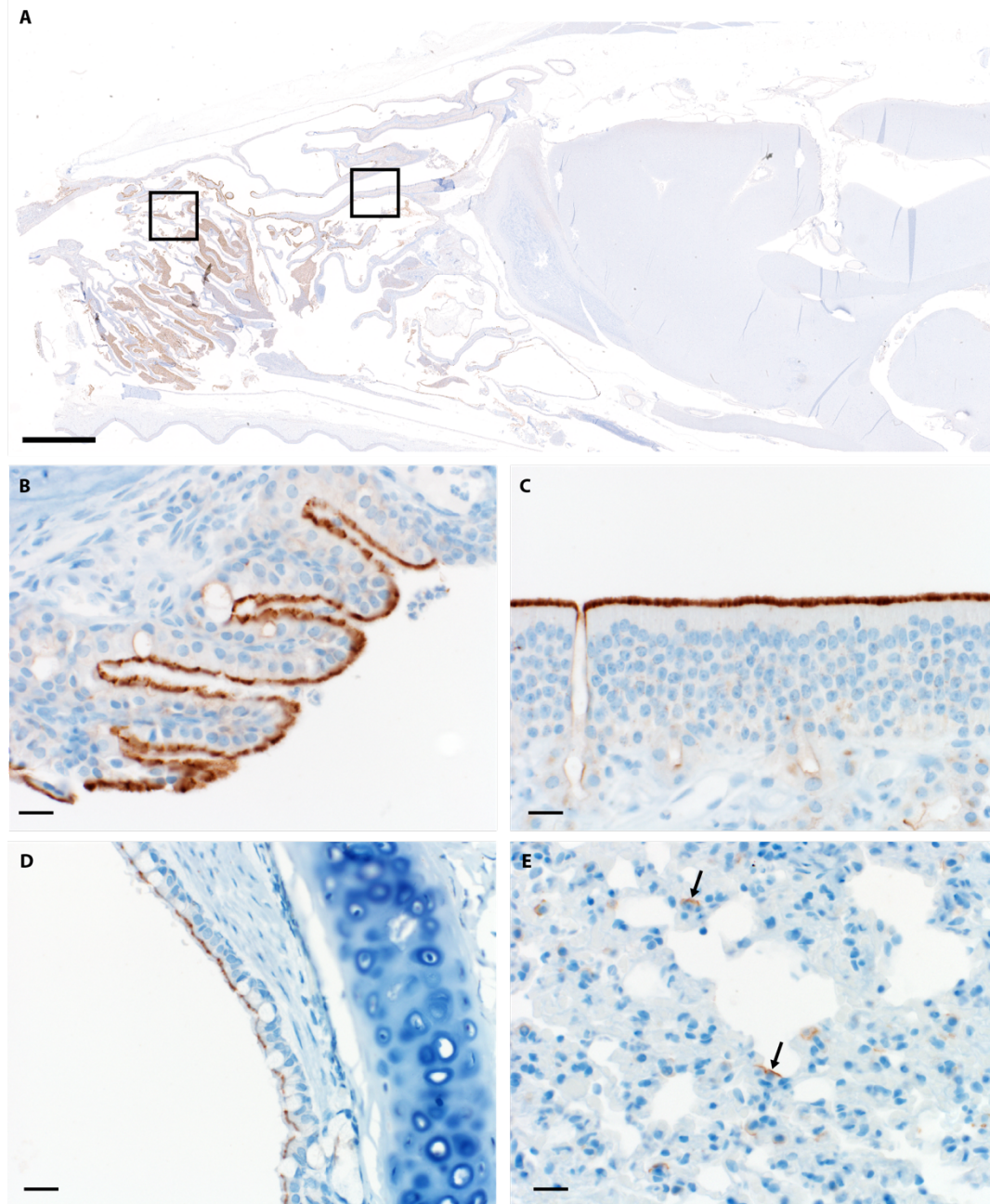
757 **Competing interests:** The authors declare no competing interests.

758

759

760

761 **Supplementary Materials**

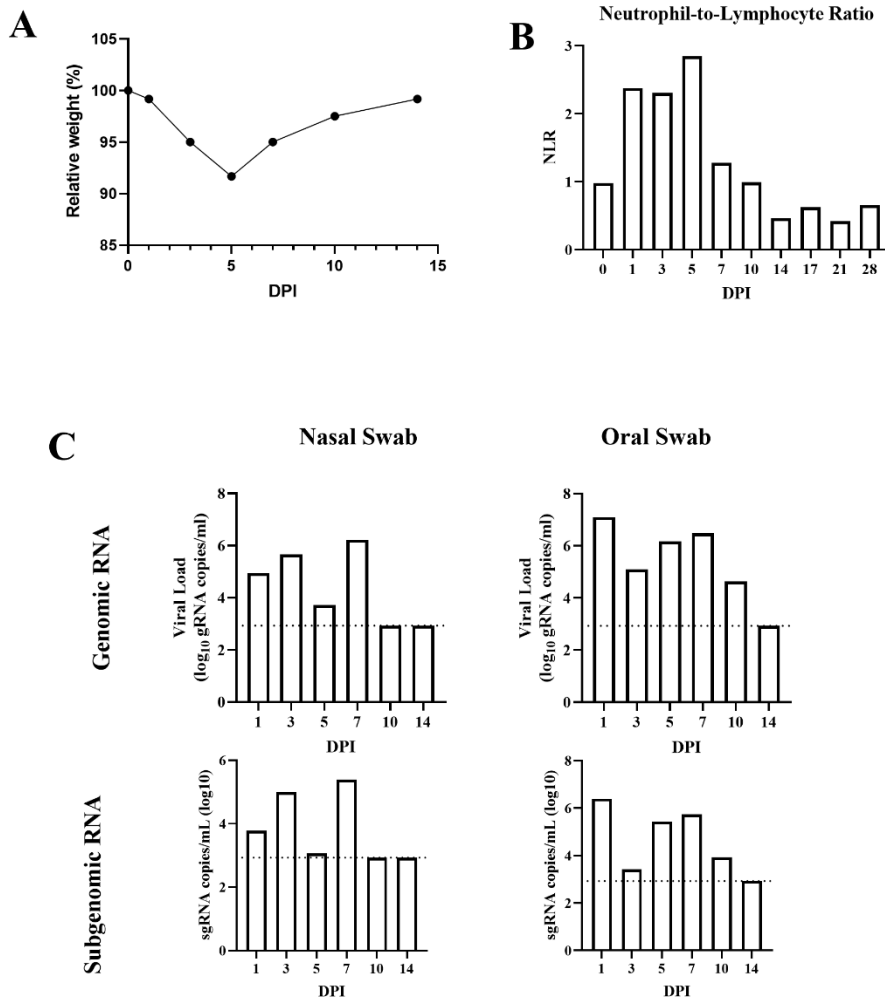


**Supplemental Figure 1. ACE2 Immunoreactivity.** (A) Sagittal section of skull ACE2 immunoreactivity (brown) bar = 3mm (B) Respiratory epithelium (C) Olfactory epithelium (D) Bronchiolar epithelium (E) Type 1 pneumocytes (arrows) Bars=20um

762

763

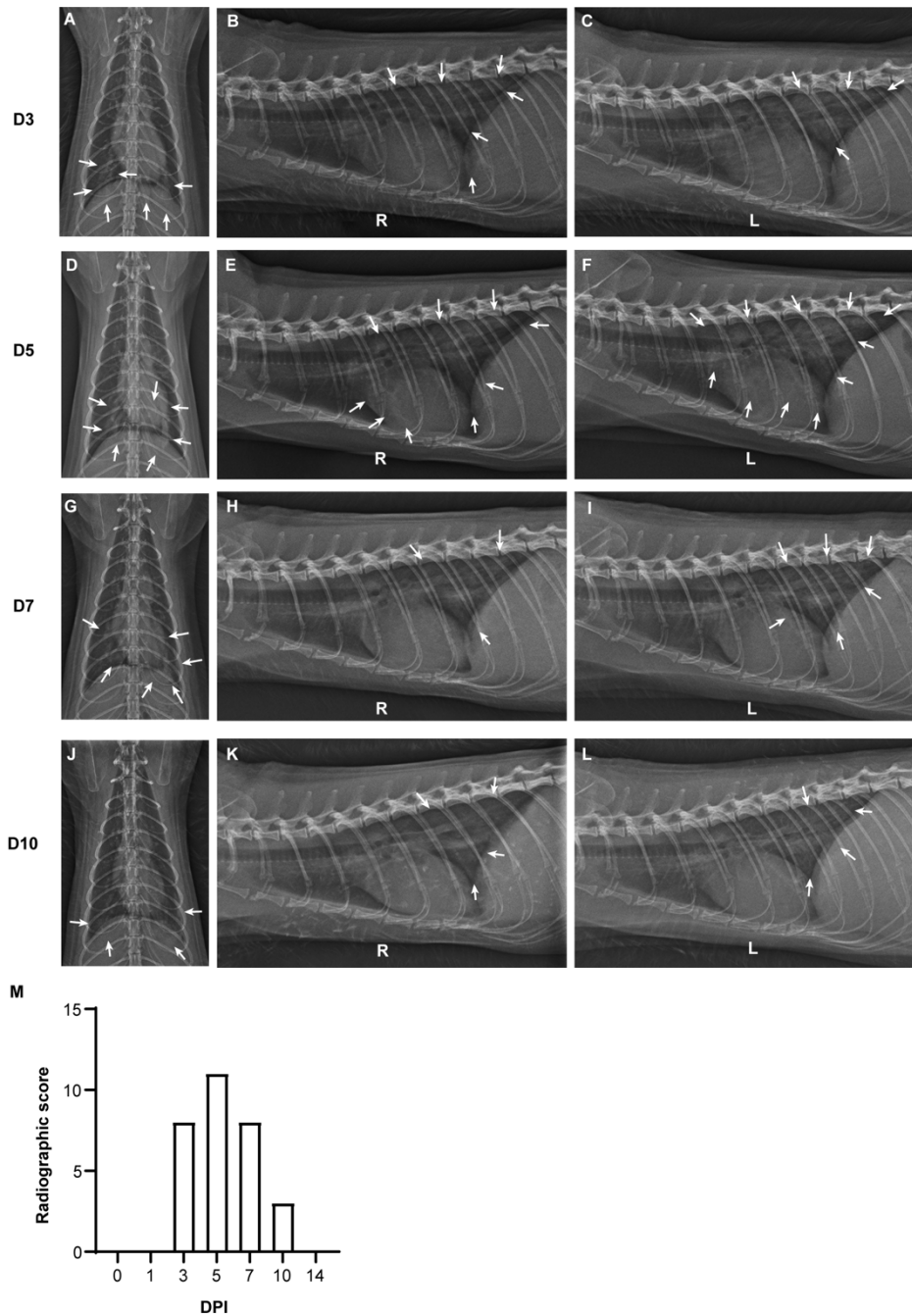
764  
765



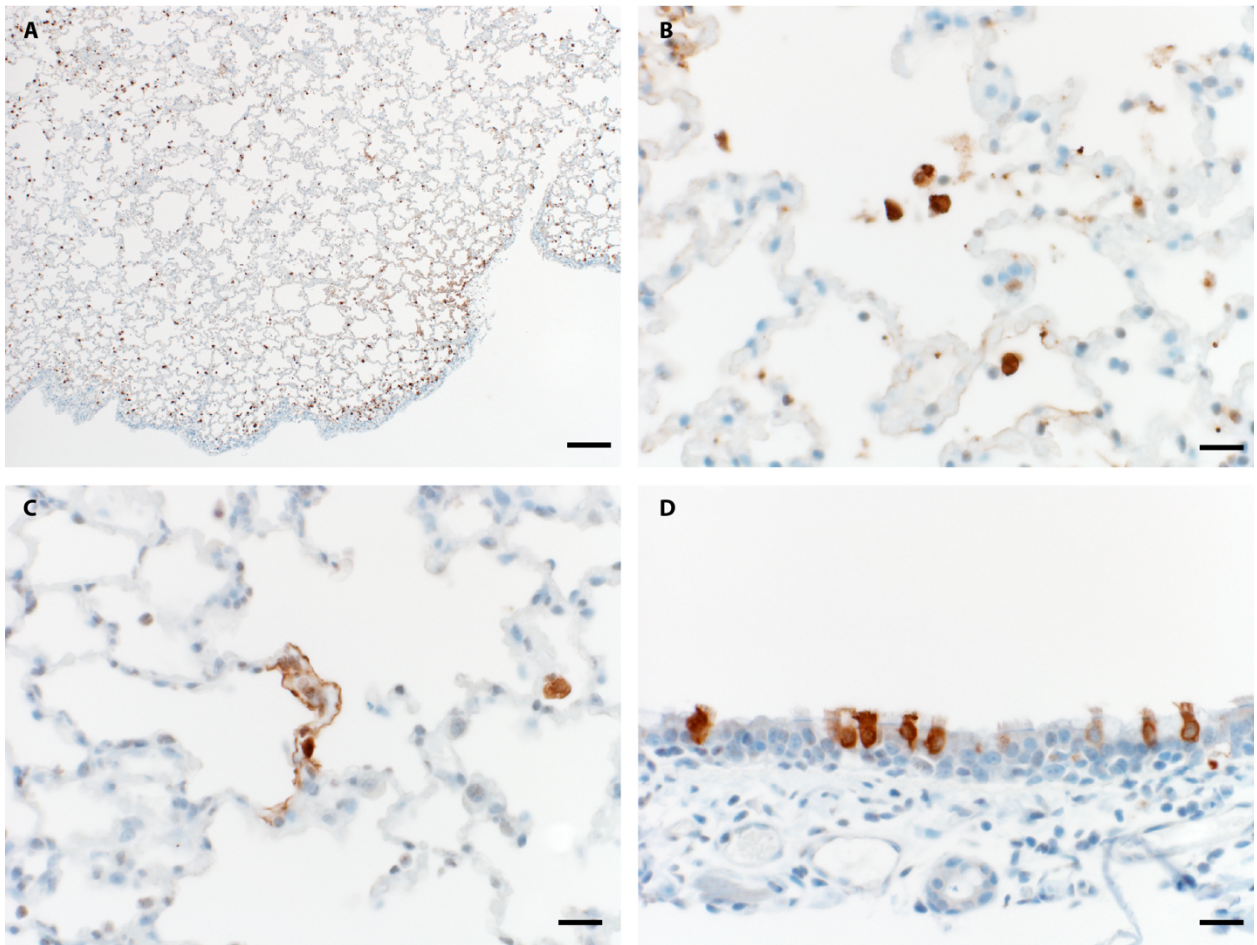
**Supplemental Figure 2. Resolution of clinical disease in the surviving animal.** The surviving animal was monitored for change in relative weight (A). Weight loss was most severe on 5 DPI, after which the animal began recovery. Neutrophil-to-lymphocyte ratio was monitored over time (B), with the most severe change appreciated on 5 DPI. Nasal and oral swabs were evaluated for resolution of viral shedding through genomic and subgenomic RT-PCR (C). All swabs on 14 DPI were below the limit of detectable virus.

766  
767  
768  
769  
770

771



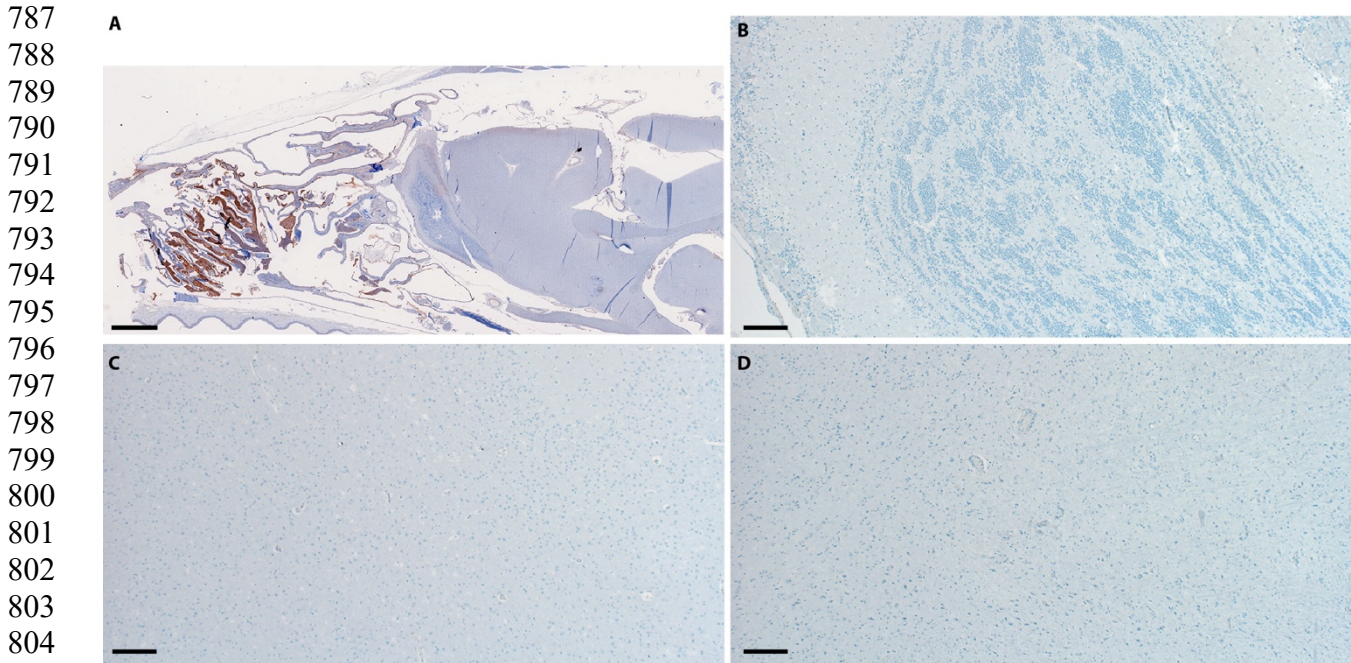
**Supplemental Figure 3. Resolution of radiological disease in the surviving animal.** (A-L) Dorsoventral, right lateral, and left lateral radiographs from surviving animal on 3, 5, 7, and 10 DPI. Arrows indicate pulmonary infiltrates, first visible in the left and right caudal lung lobes at 3 DPI (A-C) with additional involvement in the caudal subsegment of the left cranial lung lobe on 5 DPI (D-F). There is mild improvement in the alveolar pattern in the left and right caudal lung lobes on 7 DPI, with resolution in the caudal subsegment of the left cranial lung lobe (G-I). The pulmonary changes continued to improve by 10 DPI, with grade 2 pulmonary disease in the right caudal lung lobe with grade 1 pulmonary disease in the left caudal lung lobe consistent with improving viral pneumonia and pneumonitis (J-L). (M) Radiographic scores for surviving animal.



**Supplemental Figure 4. SARS-CoV-2 Pulmonary immunohistochemistry.** (A) Lung: Bar=200um (B) Alveolar macrophage immunoreactivity (C) Type I & II pneumocyte immunoreactivity (D) Bronchiolar epithelium immunoreactivity (brown=immunoreactive cells) C-E Bar=20um

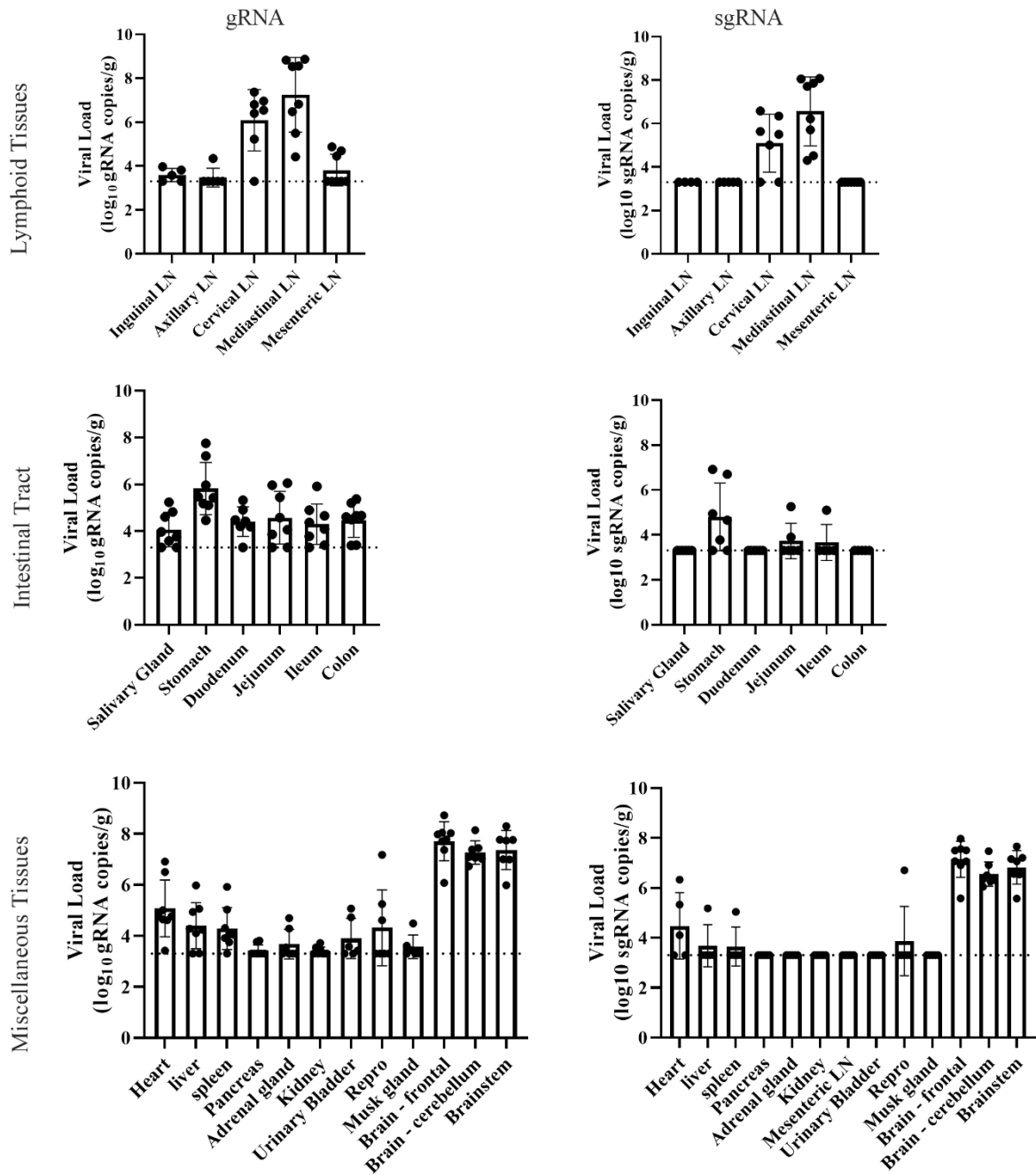
772  
773  
774  
775  
776  
777  
778  
779  
780  
781  
782  
783  
784  
785  
786





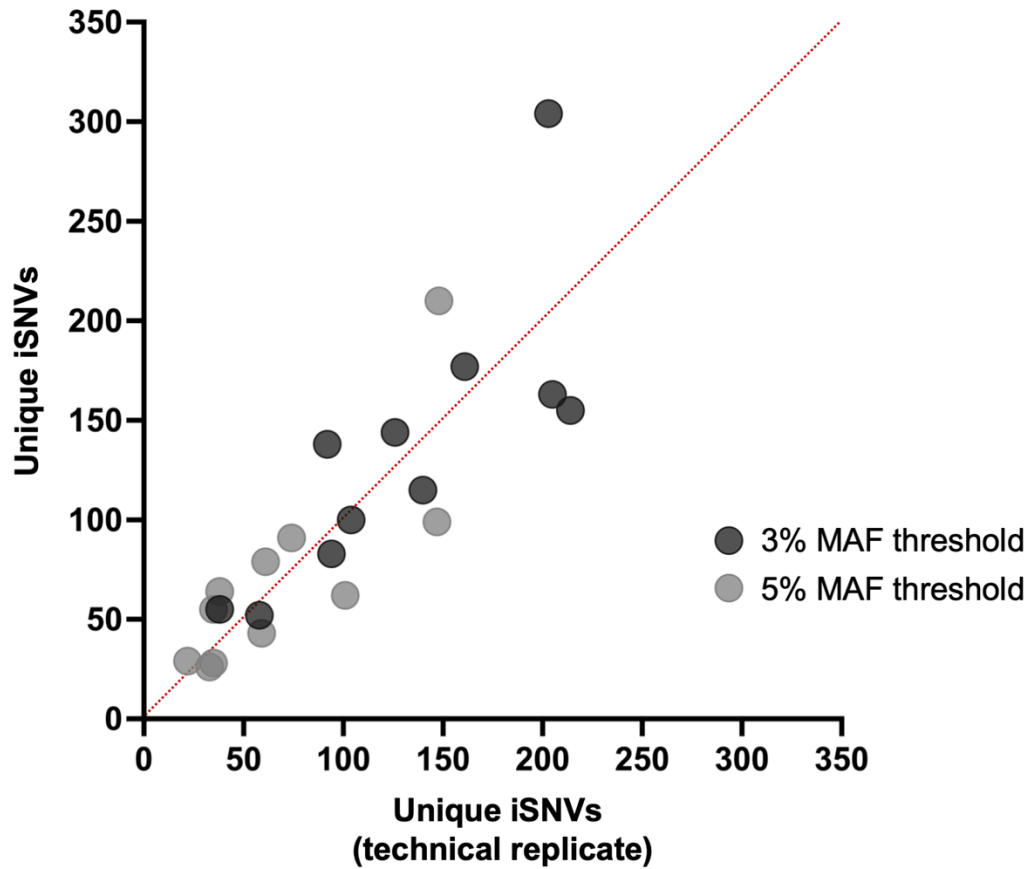
805 **Supplemental Figure 5. Nasal turbinate and brain SARS-CoV-2 immunohistochemistry.**  
806 (A) Sagittal section of skull: Abundant nasal turbinate epithelium and exudate immunoreactivity  
807 (brown); bar = 3mm (B) Olfactory bulb: no immunoreactivity (C) Cerebral cortex: no  
808 immunoreactivity (D) Brainstem: no immunoreactivity. B-D bar = 200 $\mu$ m  
809

810  
811  
812  
813  
814  
815  
816  
817  
818  
819  
820  
821  
822  
823  
824  
825  
826  
827  
828  
829  
830  
831  
832

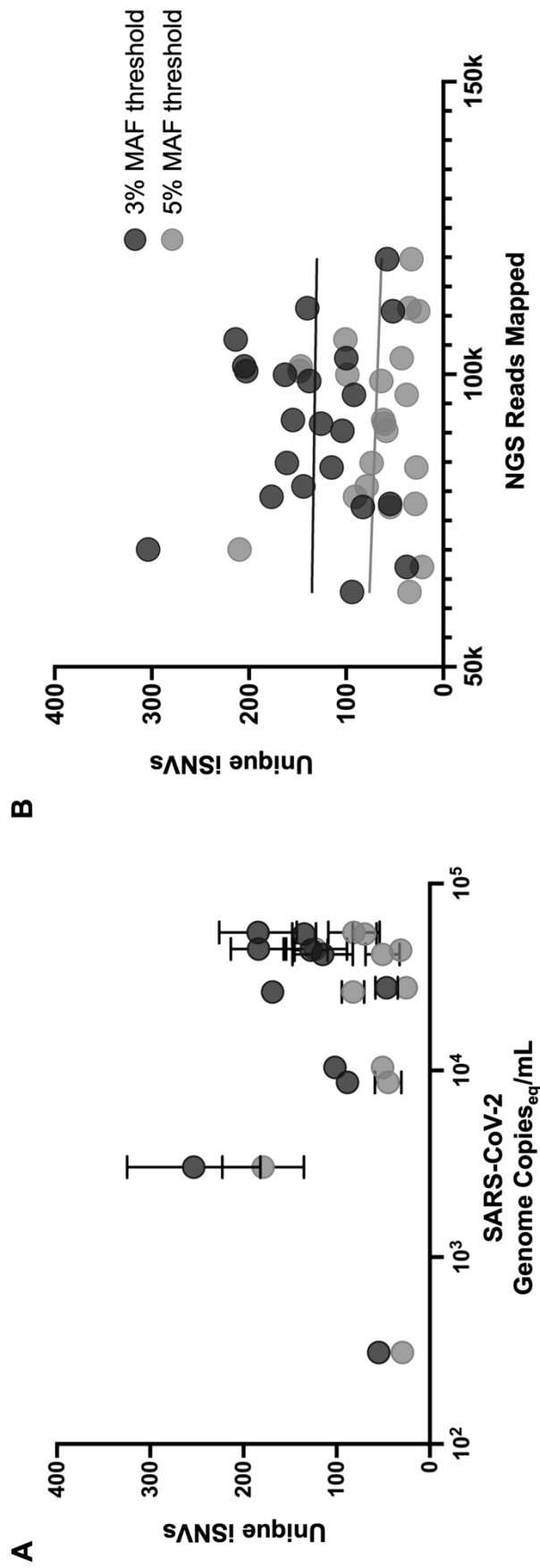


**Supplemental Figure 6. Viral burden in non-respiratory tissues.** Lymphoid (A), intestinal (B), and miscellaneous (C) tissues from animals euthanized on 3 DPI were evaluated for genomic and sub-genomic RNA. Graphs depict the mean and standard deviation.

833  
834  
835  
836  
837  
838  
839  
840  
841  
842  
843  
844  
845  
846  
847  
848  
849  
850  
851  
852  
853  
854  
855  
856  
857  
858  
859  
860  
861  
862  
863  
864  
865  
866  
867  
868  
869  
870  
871  
872  
873  
874  
875  
876  
877  
878



**Supplemental Figure 7. Comparison of intrahost single nucleotide variants (iSNVs) detected between technical replicates at minor allele frequencies (MAFs) of 3% and 5%. Dots along the red line indicate perfect concordance between replicates, whereas dots farther from the red line indicate less concordance between replicates.**



**Supplemental Figure 8 (A) Unique intrahost single nucleotide variants (iSNVs) relative to SARS-CoV-2 genome copy number or (B) number of sequenced reads mapped for each sample. Data shown for all samples with minor allele frequency thresholds of 3% and 5%.**

926  
927  
928

**Supplemental Table 1. Samples from mink experimentally challenged with SARS-CoV-2 that were deep sequenced for within-host evolutionary analyses.**

| Name              | Days Post Inoculation | Sample Type | NSP5 (Ct) | SARS-CoV-2 genome copies (eq)/mL | Reads Mapped | Reads Mapped (Technical Rep) |
|-------------------|-----------------------|-------------|-----------|----------------------------------|--------------|------------------------------|
| mink01            | 1                     | oral swab   | 25.2      | 1.82E+05                         | 82,994       |                              |
|                   | 3                     | lung tissue | 24.8      | 2.34E+05                         | 96,688       |                              |
| mink02            | 3                     | oral swab   | 25.4      | 1.59E+05                         | 73,964       |                              |
|                   | 1                     | oral swab   | 23.5      | 5.48E+05                         | 94,620       |                              |
|                   | 2                     | lung tissue | 20.5      | 3.53E+06                         | 83,812       |                              |
| mink03            | 2                     | oral swab   | 27.1      | 5.48E+04                         | 92,177       | 105,980                      |
|                   | 1                     | oral swab   | 27.1      | 5.37E+04                         | 80,835       | 91,544                       |
|                   | 3                     | lung tissue | 20.5      | 3.72E+06                         | 68,368       |                              |
| mink04            | 3                     | oral swab   | 25        | 2.08E+05                         | 87,343       |                              |
|                   | 1                     | oral swab   | 23.9      | 4.16E+05                         | 89,083       |                              |
|                   | 3                     | lung tissue | 17.9      | 1.90E+07                         | 120,414      |                              |
| mink05            | 3                     | oral swab   | 24.1      | 3.72E+05                         | 90,275       |                              |
|                   | 1                     | oral swab   | 27.5      | 4.18E+04                         | 98,844       | 96,509                       |
|                   | 3                     | lung tissue | 17.6      | 2.28E+07                         | 95,960       |                              |
| mink06            | 3                     | oral swab   | 25.1      | 1.91E+05                         | 82,691       |                              |
|                   | 1                     | oral swab   | 24.9      | 2.12E+05                         | 82,531       |                              |
|                   | 3                     | lung tissue | 16.9      | 3.59E+07                         | 83,560       |                              |
| mink07            | 3                     | oral swab   | 31.6      | 3.04E+03                         | 70,069       | 100,539                      |
|                   | 1                     | oral swab   | 23.1      | 6.73E+05                         | 82,750       |                              |
|                   | 2                     | lung tissue | 25.2      | 1.84E+05                         | 83,869       |                              |
| mink08            | 2                     | oral swab   | 29.7      | 1.04E+04                         | 102,762      | 90,328                       |
|                   | 1                     | oral swab   | 25.8      | 1.24E+05                         | 96,249       |                              |
|                   | 3                     | lung tissue | 16.6      | 4.44E+07                         | 91,707       |                              |
| mink09            | 1                     | oral swab   | 26        | 1.10E+05                         | 105,882      |                              |
|                   | 3                     | lung tissue | 16.1      | 5.93E+07                         | 70,836       |                              |
|                   | 3                     | oral swab   | 27.4      | 4.47E+04                         | 99,943       | 101,347                      |
| mink10            | 1                     | oral swab   | 27.8      | 3.32E+04                         | 77,189       | 13 (excluded)                |
|                   | 3                     | lung tissue | 28.1      | 2.77E+04                         | 77,862       | 67,088                       |
|                   | 3                     | oral swab   | 27.4      | 4.41E+04                         | 84,064       | 111,319                      |
| mink11 (survivor) | 1                     | oral swab   | 24.9      | 2.14E+05                         | 66,375       |                              |
|                   | 3                     | oral swab   | 28.2      | 2.63E+04                         | 79,066       | 84,833                       |
| Group 1           | 5                     | oral swab   | 35.2      | 3.09E+02                         | 110,791      | 119,696                      |
|                   | 7                     | oral swab   | 30        | 8.64E+03                         | 77,324       | 62,811                       |
| Group 2           | 0                     | inoculum    | 24.7      | 2.50E+05                         | 75,081       |                              |
| Group 2           | 0                     | inoculum    | 24.2      | 3.34E+05                         | 91,597       |                              |

929  
930  
931  
932  
933



980  
981  
982  
983  
984  
985  
986  
987  
988  
989  
990  
991  
992

**Supplementary Table 3: Long range PCR primers for amplification of ACE2.**

| <b>Primer</b> | <b>Sequence (5' - 3')</b>         |
|---------------|-----------------------------------|
| Amplicon 1-F  | CCCAACCCAAGTTCAAAGGCTGATGAGAGAGAA |
| Amplicon 1-R  | CTTCATGTTTAGCTATTTGACAAAGGGCTTCTT |
| Amplicon 2-F  | GGACACATCCAGTATGACATGGCATATG      |
| Amplicon 2-R  | TGGGGGAGTACAAGATTTAAGAGATTGGGAA   |

993  
994  
995  
996  
997  
998